

ELECTRICAL IMAGING OF HYPORHEIC EXCHANGE FROM  
CHANNEL-SPANNING LOGJAMS

By  
Megan Doughty

A thesis submitted to the Faculty and the Board of Trustees of the Colorado School of Mines in partial fulfillment of the requirements for the degree of Master of Science (Hydrology).

Golden, Colorado

Date \_\_\_\_\_

Signed: \_\_\_\_\_

Megan Doughty

Signed: \_\_\_\_\_

Dr. Kamini Singha  
Thesis Advisor

Golden, Colorado

Date \_\_\_\_\_

Signed: \_\_\_\_\_

Dr. Josh Sharp  
Professor and Director  
Hydrologic Science & Engineering Program

## ABSTRACT

Human impacts such as timber harvesting, engineered channels, beaver removal, and urbanization can alter the inherent characteristics and features of streams, which affect their natural physical and chemical states. One such feature substantially diminished by anthropogenic changes is the development of blockages from fallen trees and loose wood in streams. These logjams increase hydraulic resistance and create hydraulic head gradients along the streambed that drive groundwater-surface water exchange. This exchange occurs in saturated sediment under and around a stream, called the hyporheic zone, where surface water and groundwater mix. Hyporheic exchange has an important influence on a stream's ecosystem, because it transfers dissolved oxygen, solutes, and nutrients into the subsurface as well as mediates temperature fluctuations. Here, we focus on quantifying the changes in hyporheic exchange flow (HEF) due to channel-spanning logjams. Field measurements and numerical modeling using MODFLOW and MT3D were used in this study to explore logjam-induced hyporheic exchange.

The traditional methods for characterizing HEF, such as in-stream and well monitoring, fail to capture the complex hyporheic processes because they only provide point measurements. Electrical resistivity imaging (ERI), a surface-based geophysical method, was used to monitor the transport of solutes into the hyporheic zone during an in-stream tracer test supplemented by in-stream monitoring. ERI provides spatial and temporal data on the distribution of subsurface bulk electrical resistivity. We ran ERI at two reaches in Little Beaver Creek, CO: one with a single logjam and the second at a control reach with no logjams. Our results show that 1) higher HEF occurred at the reach with a logjam than the one without, and that 2) higher discharge rates associated with spring snowmelt increase the extent and magnitude of HEF, while 3) lower flows may increase the residence time in the hyporheic zone. The numerical modeling in MODFLOW and MT3D supports the finding that logjams increase the extent and rate of HEF. This research has implications for quantifying the controls of natural stream heterogeneity, the transport of sediment, the health of the stream's ecosystem, and improving stream restoration and conservation efforts.

## TABLE OF CONTENTS

LIST OF FIGURES .....	vi
LIST OF TABLES .....	vii
CHAPTER 1 INTRODUCTION .....	1
CHAPTER 2 ELECTRICAL IMAGING OF THE CHANGES IN THE EXTENT OF HYPORHEIC EXCHANGE FROM CHANNEL-SPANNING LOGJAMS ....	3
2.1 Abstract .....	3
2.2 Introduction .....	4
2.3 Background .....	6
2.3.1 Hyporheic Exchange Flow.....	6
2.3.2 Logjams.....	6
2.3.3 Mapping HEF with Geophysical Methods .....	7
2.4 Methods.....	8
2.4.1 Site Observations .....	8
2.4.2 Field Methods: Tracer Injection.....	11
2.4.3 Field Methods: Electrical Resistivity Imaging .....	12
2.5 Inversion of ER Data.....	13
2.6 Numerical Modeling of Flow and Transport.....	14
2.7 Temporal Moments .....	17
2.8 Results: Field Data .....	18
2.8.1 Control transect.....	18
2.8.2 Above the logjam.....	19
2.8.3 Below the logjam .....	21
2.9 Results: Numerical Modeling.....	25
2.9.1 No-logjam, Low-flow .....	26
2.9.2 No-logjam, High-flow.....	26
2.9.3 Logjam, Low-flow .....	27
2.9.4 Logjam, High-flow .....	28
2.10 Discussion .....	32
2.10.1 Comparison of logjam and control transects in the field .....	32
2.10.2 Comparison of high vs low flows in the field.....	34

2.10.3	Insights from numerical modeling .....	35
2.11	Conclusions .....	36
APPENDIX A	SUPPORTING FIGURES .....	44
APPENDIX B	TEMPORAL MOMENT CALCULATIONS: MATLAB FUNCTION .....	49

## LIST OF FIGURES

Figure 1.1 Cross sectional view of a flow path around a logjam.....	2
Figure 2.1 (A) Location of Little Beaver Creek, Colorado.....	9
Figure 2.2 Calculated discharge for Little Beaver Creek .....	10
Figure 2.3 Control and logjam site configuration.....	10
Figure 2.4 (A) Flow and transport model setup.....	16
Figure 2.5 Data from the three transects.....	23
Figure 2.6 Data from the three transects.....	23
Figure 2.7 Data from the three transects.....	24
Figure 2.8 Fluid and mean bulk apparent conductivity from the June 13-14 .....	24
Figure 2.9 Fluid and mean bulk apparent conductivity from the July 10-11 .....	24
Figure 2.10 Fluid and mean bulk apparent conductivity from the July 28-29.....	25
Figure 2.11 Temporal moments (mass, mean arrival time, variance, and skew) .....	25
Figure 2.12 Concentration plots (mg/L) from Modflow and MT3D.....	30
Figure 2.13 Comparison of the concentration.....	30
Figure 2.14 Bar plots of the temporal moments for the model.....	31
Figure 2.15 Concentration in the cross section along the stream. ....	32
Figure A.1 (A) Developed rating curve from stream gauging.....	44
Figure A.2 Head distribution maps.....	44
Figure A.3 Head distribution maps.....	46
Figure A.4 Map view of the concentration plot.....	46
Figure A.5 Map view of the concentration plot.....	47
Figure A.6 Concentration (mg/L) in stream from the four models.....	47

## LIST OF TABLES

Table 2.1 Details of tracer tests.....	11
Table 2.2 Model Properties.....	15
Table A.1 Temporal Moment Calculations for Fluid Conductivity .....	45
Table A.2 Temporal Moment Calculations for Bulk Conductivity .....	45
Table A.3 Site A, Site B, and Site C Temporal Moments .....	48

## CHAPTER 1

### INTRODUCTION

Mountain streams are a critical component of larger river networks because of their retention and transmission of sediment and nutrients, which downstream rivers rely upon for healthy ecosystems and sediment supply, and the provision of critical habitats and refuge for aquatic organisms. Small streams and headwaters are frequently under-regulated and neglected because many do not realize their ecological significance (Wohl, 2017). Additionally, first-, second-, and third-order streams make up 75-85% of the total channel length in river networks (Downing et al., 2012). Mountain streams and headwaters also respond rapidly and drastically to changes in land use or atmospheric changes, because they are close to their flow inputs with none of the buffering capabilities of downstream rivers (Wohl, 2017). This sensitivity and lack of regulation means that headwater and mountain streams are at high risk from human-induced change. Therefore, scientific understanding of stream form and function is critical to improve the protection, conservation, and restoration of these areas as well as downstream water quality.

This thesis specifically focuses on the impact channel-spanning logjams have on groundwater-surface water exchange in mountain streams. A zone of saturated sediment surrounds rivers and streams, and flow from the stream enters the subsurface, mixes and exchanges with groundwater, and then returns to the stream. The area where groundwater becomes surface water and becomes groundwater again is called the hyporheic zone and flow here is driven by spatial and temporal changes in a stream. Logjams create blockages within a channel, which causes pooling behind the jam and the development of a head gradient along the streambed. This head gradient drives water from the stream into the hyporheic zone and then water returns to the surface farther downstream (Figure 1.1). The hyporheic zone provides an area for important biogeochemical processes such as the transfer of solutes and nutrients from the stream into the subsurface, regulation for stream temperatures, and habitable environments for microorganisms and macroinvertebrates. These functions are critical for healthy ecosystems and better water quality. While the focus of this study is the impact of logjams on hyporheic exchange, logjams have other benefits to mountain streams such as providing diverse habitats, reducing large fluxes of water moving downstream, and contributing to stream complexity.

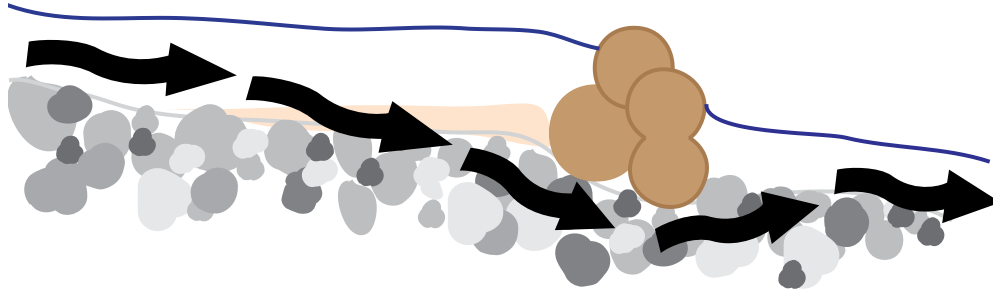


Figure 1.1 Cross sectional view of a flow path around a logjam. The arrows show the potential movement of a water particle as it enters the hyporheic zone, moves through the subsurface, and then reenters the stream downstream from the logjam.

## CHAPTER 2

### ELECTRICAL IMAGING OF THE CHANGES IN THE EXTENT OF HYPORHEIC EXCHANGE FROM CHANNEL-SPANNING LOGJAMS

#### 2.1 Abstract

Human impacts such as timber harvesting, engineered channels, beaver removal, and urbanization can alter the inherent characteristics and features of streams, which affect their natural physical and chemical states. One such feature substantially diminished by anthropogenic changes is the development of blockages from fallen trees and loose wood in streams. These logjams increase hydraulic resistance and create hydraulic head gradients along the streambed that drive groundwater-surface water exchange. This exchange occurs in saturated sediment under and around a stream, called the hyporheic zone, where surface water and groundwater mix. Hyporheic exchange has an important influence on a stream's ecosystem, because it transfers dissolved oxygen, solutes, and nutrients into the subsurface as well as mediates temperature fluctuations. Here, we focus on quantifying the changes in hyporheic exchange flow (HEF) due to channel-spanning logjams. Field measurements and numerical modeling using MODFLOW and MT3D were used in this study to explore logjam-induced hyporheic exchange.

The traditional methods for characterizing HEF, such as in-stream and well monitoring, fail to capture the complex hyporheic processes because they only provide point measurements. Electrical resistivity imaging (ERI), a surface-based geophysical method, was used to monitor the transport of solutes into the hyporheic zone during an in-stream tracer test supplemented by in-stream monitoring. ERI provides spatial and temporal data on the distribution of subsurface bulk electrical resistivity. We ran ERI at two reaches in Little Beaver Creek, CO: one with a single logjam and the second at a control reach with no logjams. Our results show that 1) higher HEF occurred at the reach with a logjam than the one without, and that 2) higher discharge rates associated with spring snowmelt increase the extent and magnitude of HEF, while 3) lower flows may increase the residence time in the hyporheic zone. The numerical modeling in MODFLOW and MT3D supports the finding that logjams increase the extent and rate of HEF. This research has implications for quantifying the controls of natural stream heterogeneity, the transport of sediment, the health of the stream's ecosystem, and improving stream restoration and conservation efforts.

## 2.2 Introduction

As drainage features, rivers provide vital aquatic habitats, route floodwater, and provide downstream river networks with essential nutrients and sediments, but they are also subject to disturbances from land-use and atmospheric changes in their catchments (e.g., Bernhardt and Palmer, 2007). Human activities such as timber harvesting, stream engineering, urbanization, beaver removal, and climate change have a substantial impact on rivers. These activities have become widespread throughout industrialized countries and altered hydrogeologic processes from headwaters to regional scales; for example, for the past two centuries in the western United States, people have manipulated streams and rivers to control flow, simplify channels, and homogenize water and sediment movement. A common method for “improving” a stream was to clear channels of obstructions such as boulders, leaning trees, or sunken logs to allow for easier timber conveyance and transportation (Sedell et al., 1991). While natural variability and seasonal flows deposit and erode sediment, create channel features, and increase floodplain and channel connectivity (e.g., Allan, 2004), direct and indirect human alterations substantially reduce the inherent complexity and diversity of river form and function (e.g., Wohl, 2005). The Front Range rivers of the Colorado Rocky Mountains have experienced 200 years of human land-use changes and provide a historical look at how these alterations result in compromised river functions (Wohl, 2005).

Controlling or interfering with flow and natural stream processes such as removing wood may have a negative impact on the transport of sediments and the health of the stream’s ecosystem (e.g., Wohl, 2005; Poff et al., 2007). Benefits from in-stream wood, or logjams, include increased channel complexity from the formation of anabranching channels, increased connectivity with the floodplain, control of downstream fluxes, storage of sediment and organic material, and enhanced habitat diversity (e.g., Palmer et al., 2010; Sear et al., 2010; Livers and Wohl, 2016). Large wood, in particular, is an important aspect in river systems and impacts stream geomorphology, hydrology, and ecology (e.g., Millington and Sear, 2007). Additionally, logjams can create hydraulic head variations along the river’s flow path (e.g., Manners et al., 2007; Buffington and Tonina, 2009), increasing the hydraulic resistance and driving groundwater-surface water exchange (e.g., Wondzell, 2006; Buffington and Tonina, 2009). Surface water that moves into the alluvium via downwelling and then returns to the river farther downstream via upwelling defines hyporheic exchange flows (HEF; Tonina and Buffington,

2009). Hyporheic exchange has a substantial influence on a stream's ecosystem, because it transfers dissolved oxygen, solutes, and nutrients into the subsurface as well as buffers stream-temperature fluctuations (e.g., Fanelli and Lautz, 2008). Many different factors influence the extent and amount of HEF in a stream such as geomorphological features, underlying sediment, seasonal fluctuations in flow, and flow obstructions (e.g., Tonina and Buffington, 2009) such as in-stream wood. Timber harvesting has changed runoff patterns and decreased the availability of in-stream wood (Wohl and Beckman, 2014). When there is less vegetation to intercept precipitation, take up water, or stabilize slopes, sediments are more easily eroded and deposited into those streams (e.g., Campbell and Doeg, 1989). Streambed clogging and siltation reduce the amount and activity of hyporheic invertebrates (Hancock, 2002). Clearing in the riparian area also decreases the available in-stream wood, reducing stream complexity favorable for inducing HEF, and decreases stream shading, which increases temperatures in the stream and hyporheic zone (e.g., Allan, 2004; Sweeney and Newbold, 2014), altering the biogeochemical processes that occur there.

Here, we focus on quantifying the changes in HEF relating to channel-spanning logjams at different stream discharges. Many field studies of HEF have focused on unjammed streams, as these are more prevalent where channel clearing is practiced. Relatively little is known about the impact of logjam presence and density on HEF. We expect an increase in HEF extent in a reach with a logjam compared to a similar reach with no jam, because the flow obstruction will increase downwelling. We also anticipate an increase in HEF during peak snowmelt, regardless of jams (Loheide and Lundquist, 2009), but a greater change in HEF should occur in streams impacted by logjams due to the large head gradient across the jams under high flow. To explore these expected behaviors, we conducted field measurements and numerical modeling of two stream reaches, one without a logjam, which serves as a control, and one with a channel-spanning logjam. We performed tracer tests at the reaches of interest using dissolved NaCl as a conservative solute. Additionally, NaCl is electrically conductive, which allows it to be visible to geophysical methods such as electrical resistivity (ER), which we use here, for the first time, to characterize changes in HEF due to logjams. Numerical modeling, using MODFLOW and MT3DMS, provides additional insight beyond the field measurements and helps to quantify the relationship between logjams and HEF.

## **2.3 Background**

### **2.3.1 Hyporheic Exchange Flow**

Quantifying changes in hyporheic exchange is important for improving water quality, regulating stream temperature, and maintaining hospitable environments for microorganism and macroinvertebrates (e.g., Tonina and Buffington, 2009). As surface water moves into the subsurface and mixes with the groundwater, the downstream movement of solutes is slowed and residence time of waters in the stream system increases (Lautz et al., 2006). Downwelling supplies organic materials and dissolved oxygen to the hyporheic zone, which creates aerobic environments for invertebrates and microbes, and improves hyporheic productivity (Tonina and Buffington, 2009; Boulton et al., 2010). HEF also creates localized thermal refuges (Sawyer and Cardenas, 2012), which are important for organism survival during disturbances such as floods, droughts, or climate change. The ability to remove pollutants is why the hyporheic zone has also been equated to a “river’s liver” (Fischer et al., 2005).

Studies have shown that the 95% of HEF is confined to a depth approximately equal to the width of the channel in unimpeded streams and becomes shallower with steeper slopes (Marzadri et al., 2010). However, the extent and magnitude of HEF is driven by subsurface head distributions, which are controlled by geomorphic and hydrologic conditions in streams and rivers (Gooseff et al., 2006), including streambed heterogeneity and hydraulic conductivity, stream meanders, bedforms (e.g., Cardenas et al., 2004; Hester and Doyle, 2008), changes in discharge (Wroblicky et al., 1998), and bed topography (Harvey and Bencala, 1993). Stream discharge controls the hydraulic head distribution across streambed sediments (Tonina and Buffington, 2011), and generally increases HEF during snowmelt flows (Lautz et al., 2006). Sediment heterogeneity also creates head variations and subsurface preferential pathways, which can increase stream water flux into the hyporheic zone (Salehin et al., 2004). Studies looking at variable bed topography have shown that stream water downwells at the downstream end of pools, stays in the hyporheic zone, and then upwells at the upstream end of the next pool (Harvey and Bencala, 1993).

### **2.3.2 Logjams**

Logjams typically form from either the accumulation of woody and organic material suspended in a stream or from the falling of a tree and subsequent entrapment of woody and

organic materials, which range in size from leaves and twigs to whole tree trunks (e.g., Curran and Wohl, 2003; Manners et al., 2007). The jam itself can vary in size, shape, and porosity depending on the wood matrix and composition of woody material. Studies in Rocky Mountain streams observed that although individual pieces of wood move in streams during most years, the location of logjams and the wood load stay relatively constant (Wohl and Goode, 2008). Therefore, the makeup of logjams fluctuates throughout the season with wood accumulation and discharge variations (Manners et al., 2007), but the jam may be a relatively persistent feature of the stream for long periods of time. Other observations in the Southern Rockies have found that riparian forest age, management history, and valley geometry influences the characteristics and amount of wood and logjams (e.g., Livers and Wohl, 2016).

The channel obstruction causes water to build up behind the logjam to create slower moving pools and secondary channels, which is important for creating diverse habitats and encouraging biodiversity (e.g., Buffington et al., 2002; Palmer et al., 2010; Livers and Wohl, 2016). More abundant in-stream wood has been shown to correlate with larger pool volumes and greater sediment storage (Wohl and Scott, 2017). Thick stratified beds of sediment increase the development of horizontal flow paths in the subsurface (Marion et al., 2008), which often form behind logjams (Wohl and Scott, 2017).

Logjams contribute to forming many of the conditions conducive for advection-induced HEF (Lautz et al., 2006), such as topography variability with downwelling in the above the jam pool and upwelling further downstream. HEF rates are highest near the logjams and decrease exponentially with distance upstream and downstream (Sawyer et al., 2011). Logjams also create substantial head gradients due to the change in head across the obstruction (Manners et al., 2007; Buffington and Tonina, 2009; Sawyer et al., 2011), which increases as more of the flow is obstructed (Hester and Doyle, 2008; Sawyer et al., 2011). We therefore focus on channel-spanning logjams, which block large portions of the channel cross-section. Logjams also alter the thickness and grain-size distribution of alluvial bed substrate, which effect HEF.

### **2.3.3 Mapping HEF with Geophysical Methods**

Our ability to quantify HEF is limited by our ability to explore subsurface processes. Many studies have interpreted the amount of HEF or the associated residence time in the hyporheic zone using tracer tests and in-stream monitoring techniques or well networks (e.g.,

Wörman et al., 2002; Anderson et al., 2005; Lautz et al., 2006; Wondzell, 2006; Tonina and Buffington, 2007). From these measurements, inferences of HEF have been made using numerical modeling and/or breakthrough curve interpretations. One issue with these methods, however, is the limitation of point measurements, which cannot capture the complex, spatial heterogeneity inherent in HEF. Electrical resistivity (ER) has been extensively used in recent studies to characterize surface water-groundwater interactions (Singha et al., 2010; Slater et al., 2010; Ward et al., 2010b, 2010a; Cardenas and Markowski, 2011; Coscia et al., 2011; Toran et al., 2012 ), because it provides spatial and temporal data on the subsurface bulk electrical resistivity, which is sensitive to rock type, porosity, total dissolved solids, and geologic material. In a time-lapse mode, the background conditions should difference out, making ER a valuable method for characterizing hydrologic processes (Ward et al., 2010b; Cardenas and Markowski, 2011; Coscia et al., 2011). Use of an electrically conductive, conservative tracer, such as NaCl, in conjunction with ER, has been able to successfully assess the hyporheic zone through many field experiments (Ward et al., 2010a, 2010b; Toran et al., 2013; Ward et al., 2014;).

## **2.4 Methods**

### **2.4.1 Site Observations**

We conducted all field measurements along two segments of Little Beaver Creek, a third-order tributary to the South Fork of the Cache la Poudre River in northern Colorado (Figure 2.1). The creek has an average channel width of 6 m and a slope of 0.02 through the reaches of interest. This creek sits within the montane forest zone dominated by ponderosa pine, and the riparian zone contains ponderosa pine, Douglas-fir, Engelmann spruce, and aspen. The drainage area (40 km<sup>2</sup>) sits at a high elevation of 1830-2740 m, and is snowmelt dominated (Jarrett, 1990). Therefore, peak flows in Little Beaver Creek occur in the spring during snowmelt and decrease throughout the summer (Figure 2.2), although discharge may increase during and after rainfall. While spring runoff and summer floods can move large wood pieces and sometimes remove logjams, the jams at this site have remained relatively constant from year to year based on our observations. We focus on two reaches along Little Beaver Creek in this study: a logjam and control transect.

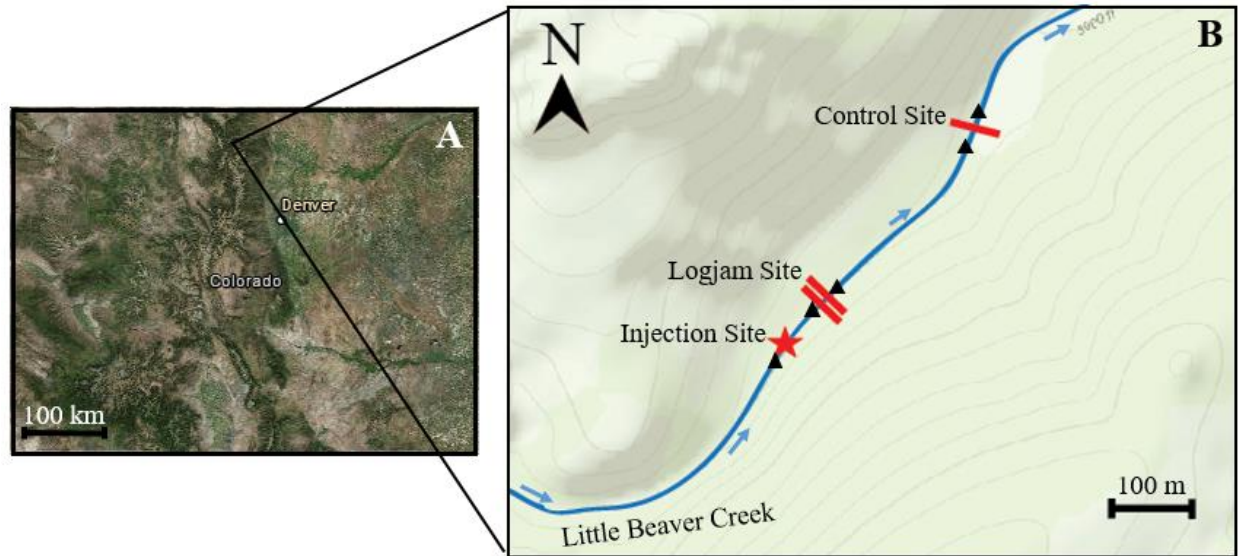


Figure 2.1 (A) Location of Little Beaver Creek, Colorado. (B) The inset map shows the location of the injection site (red star) relative to the ER transects (red lines) and the in-stream fluid electrical conductivity monitoring (black triangles) at the logjam and control transects. The ER transects indicated on this map are not to scale.

The logjam site is composed of a single channel-spanning logjam and single channel (Figure 2.3). A single tree makes up the key piece of the jam with other loose wood and organic material built up behind and around it. Looking downstream, the right bank of the site is highly vegetated and we observed very moist soils there as well as some standing water, particularly during high flows. The left bank is steeper with less vegetation. The control transect has no logjams within the reach and has a single channel (Figure 2.3). Both banks are highly vegetated with slightly more vegetation on the left bank. An old beaver dam and streambed were observed approximately 100 m past the left bank of the control transect. This streambed and beaver dam are no longer active.

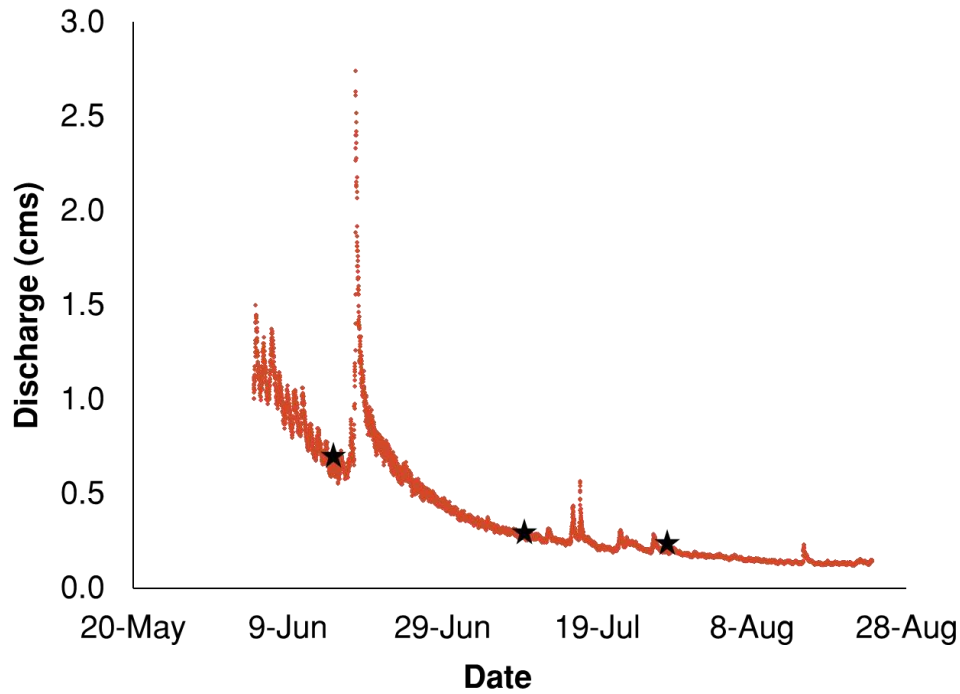


Figure 2.2 Calculated discharge for Little Beaver Creek based on in-stream stage measurements and a rating curve developed for the site. The three black stars on the graph indicate the date and flow of the three tracer tests conducted.

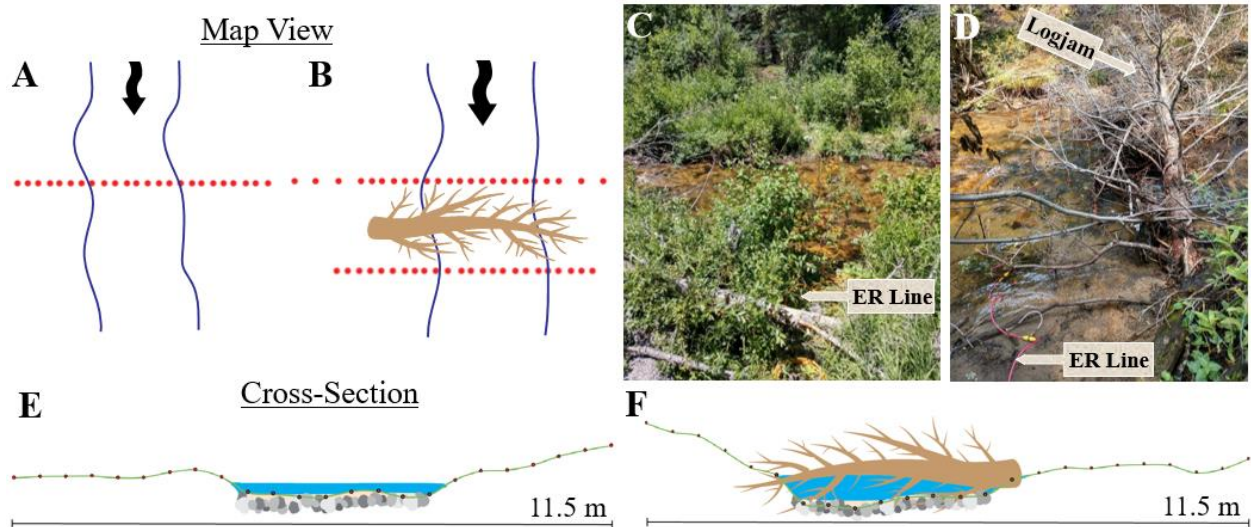


Figure 2.3 Control and logjam site configuration. (A, B) Map views of the ER lines and associated electrodes perpendicular to the stream. (C, D) Field photos of the control and logjam sites, where ER lines can be seen. (E, F) Cross-section views looking downstream, showing relative positions of the electrodes along the above-logjam transect and the relative location of the electrodes represented by red dots.

### 2.4.2 Field Methods: Tracer Injection

We conducted three constant-rate injections of dissolved NaCl (Table 2.1) for 4 hours upstream of the logjam and control transects (Figure 2.3). The tracer was pumped into Little Beaver Creek at the injection site (Figure 2.1) at a low-flow rate relative to stream discharge while in-stream and ER measurements were continuously collected. The first tracer test was conducted on June 13, 2017, during peak snowmelt runoff, at a measured flow of 0.76 cms. The second was done later in the season, on July 10, with a measured flow of 0.17 cms. The third was completed on July 28 with a measured flow of 0.18 cms. For each test, the tracer was injected at a single location at a constant rate of  $1.2 \times 10^{-4}$ ,  $3.0 \times 10^{-5}$ , and  $2.1 \times 10^{-5}$  cms from well-mixed reservoirs of constant concentration. The background fluid electrical conductivity (EC) in the stream was approximately 15.8, 21.6, and 24.9 uS/cm on the three dates, so the concentration and amount of tracer injected into the stream were calculated to increase in-stream EC by 50 uS/cm at each time based on the flow. The injection sites were approximately 50 and 250 m upstream, respectively, of the two monitored sites to allow the tracer to mix fully into the stream. The stream was monitored before the tracer test and for a minimum of 24 hours after injection using in-stream fluid EC transducers above the injection point and above and below the monitored sites (Figure 2.1).

Table 2.1 Details of tracer tests. Stream discharge was measured using stream gauging and a stilling well. Mean tracer EC is measured inside of the injection tubs before injection into the stream.

Test Date	Stream discharge (cms)	Background Stream EC (uS/cm)	Tracer Injection Rate (cms)	Mean Tracer EC (mS/cm)	Total Mass of Tracer Injected (kg)
June 13-14, 2018	0.76	15.8	$1.2 \times 10^{-4}$	228.1	318
July 10-11, 2018	0.17	21.6	$3.0 \times 10^{-5}$	240.8	91
July 28-29, 2018	0.18	24.9	$2.1 \times 10^{-5}$	242.5	79

### 2.4.3 Field Methods: Electrical Resistivity Imaging

ER is a direct-current method that can be used to estimate the spatial and temporal changes in subsurface bulk electrical conductivity. ER passes low-frequency alternating current through a pair of electrodes, which are placed into the ground. The subsequent voltage is measured in another two electrodes. This process proceeds down the ER line using different combinations of electrodes, allowing collection of hundreds of measurements in minutes. The injection of a highly conductive fluid, such as dissolved NaCl, increases the bulk conductivity of the subsurface, so ER measurements can provide a multidimensional look at the salt distributions in the subsurface through time, and consequently serve as a useful supplement to point-based fluid EC breakthrough curves.

ER data were collected using an IRIS Syscal Pro Resistivity Meter, using a dipole-dipole geometry and 24 electrodes with 0.5- to 1-m spacing (Figure 2.3), collecting 231 measurements per time step. The survey times for the transects were approximately 8 minutes long, which allowed for high resolution time-lapse data of the tracer transport. Three transects were monitored during the first three tracer tests: two were located above and below the logjam being monitored and the third was located at the control transect (Figure 2.3). Background ER data were collected for a minimum of 1 hour before the injection began along the transects. Data collection continued during and then after the 4-hour tracer injection for at least 24 hours to monitor the tracer entering and leaving the subsurface. During data collection, two replicate measurements were collected and averaged. The mean standard deviation across all measurements was 0.23%.

The bulk apparent conductivity,  $\sigma_a$ , was calculated from the measured resistance data ( $V/I$ ) using equation (2.1) and the geometric factor,  $K$ , in equation (2.2), which accounts for the arrangement of electrodes:

$$\sigma_a = \frac{I}{VK} \quad (2.1)$$

$$K = \frac{2\pi}{\frac{1}{AM} + \frac{1}{AN} + \frac{1}{BM} + \frac{1}{BN}} \quad (2.2)$$

where  $I$  is the current injected into the ground (amperes),  $V$  is the voltage measured (volts), and  $A$  and  $B$  are the current electrodes and  $M$  and  $N$  are the potential electrodes that the IRIS uses.

In order to compare the breakthrough curves from the in-stream monitoring and the ER, we averaged the calculated bulk apparent conductivity of each survey to create a composite “breakthrough curve” for the bulk conductivity.

## 2.5 Inversion of ER Data

Resistance data were inverted using the code R2 (v 3.1). R2, an inverse solution accounting for 2D current flow, is an algorithm based on Occam’s solution, as described by Binley and Kemna (2005). All four boundary conditions of the mesh are zero flux and the right, left, and lower boundaries are set a substantial distance from the area of investigation. A time-lapse inversion was used, which provides the percent difference from the background data such that errors related to field configuration and discretization are minimized (LaBrecque and Yang, 2009). Inversions based on background measurements were used as the starting model for all data collected.

The resolution matrix was also calculated; this shows how well the ER data resolved during the inversion. The resolution matrix (R) is computed for a converged solution on the background ER measurements. A complicated function of multiple factors is used for the calculation including electrode layout, measurement scheme, data signal-to-noise ratio, resistivity distribution, and the parameterization and regularization used in the inversion (Binley and Kemna, 2005). The equation for the resolution matrix from Binley and Kemna (see equation 5.18, 2005) is as follows:

$$R = (J_k^T W_d^T W_d J_k + \alpha W_m^T W_m)^{-1} J_k^T W_d^T W_d J_k \quad (2.3)$$

where k is the final inversion iteration, T is a function of the given layer thickness and resistivities, d is the data,  $J_k$  is the Jacobian matrix for the current model m,  $W_d$  is the data weighting matrix associated with individual data errors,  $W_m$  is the model weighting matrix, and  $\alpha$  is the regularization parameter. A value close to 1 indicates that the parameter for that element was resolved perfectly. As the values decrease, the resolution does as well. Values near zero indicate parameters that cannot be uniquely resolved. In general, resolution decreases with distance and depth from the electrodes.

## 2.6 Numerical Modeling of Flow and Transport

The flow and transport of an idealized, straight channel and stream corridor was modeled to explore potential changes in HEF due to changes in stream flow and logjams. A steady groundwater flow model was built using MODFLOW (Arlen, 2005), and transient solute transport was modeled using MT3DMS (Zheng and Wang, 1999) to mimic solute tracer injections. We solved transient groundwater flow and advection-dispersion equations simultaneously, but the flow field remained steady. We explored four model configurations: 1) no logjam at high flow, 2) single logjam at high flow, 3) no logjam at low flow, and 4) single logjam at low flow. As in field experiments, the simulated tracer test is represented as a continuous injection for 4 hours at fixed concentration. It is assumed that the tracer is conservative and nonreactive.

The model domain consists of three homogeneous, isotropic material types intended to represent soil, alluvium, and bedrock (Figure 2.4; Table 2.2). The soil layer is 1 m deep and has a relatively high hydraulic conductivity (8 m/d). It also contains the stream and logjams, which are defined with separate hydraulic conductivities. The stream was prescribed as a high hydraulically conductive and porous layer ( $1 \times 10^6$  m/d; a porosity of almost 1). The logjam in the model configuration is represented by an estimated hydraulic conductivity and porosity from visual field estimation (Table 2.2). Because it is difficult to determine the hydraulic conductivity for the logjam in the field, we calculated a value using Darcy's law and our numerical model, where the discharge was calculated in the no-logjam numerical model, the cross-sectional area ( $A$ ) was of the modeled stream ( $0.9 \text{ m}^2$ ), and the head drop ( $dh$ ) was 0.5 m across a 1 m distance ( $dL$ ). The stream is 0.1 m lower in elevation than the surrounding material in the upper layer. The cross-section dimensions are 0.9 m deep and 1 m wide (Figure 2.4B). After the soil, the alluvium is represented by the next 5 m at lower hydraulic conductivity than the top layer (1 m/d), which has a 1 m discretization (layers 2-6). The bottom layer is 5 m thick and represents the hydraulic conductivity of a highly fractured bedrock ( $5 \times 10^{-4}$  m/d). The entire domain is 70 m in the downstream direction ( $X$ ), 30 m in the cross-valley direction ( $Y$ ), and 11 m in the vertical ( $Z$ ). Cell sizes are 1 m (in  $X$ ,  $Y$ , and  $Z$ ) in the first 6 layers and increase to 1 by 1 by 5 m (in  $X$ ,  $Y$ , and  $Z$ ) in the 7th layer.

The groundwater flow model was run in the first stress period at steady state before the four-hour long tracer test began in the second, transient time period, and then monitored for 100

days after the injection in the third, transient time period. Along the stream surface, hydraulic head was set to vary under high-flow scenarios from 13.8 m at the top of the reach to 11 m at the bottom, leading to an overall hydraulic gradient of 0.02. Under low-flow scenarios, head varied from 11.7 to 11 m, leading to a lower gradient of 0.01. The upstream and downstream sides of the model were set to constant head values equal to head at the upstream and downstream ends of the channel (no vertical flow). The other model sides, top, and bottom were defined as no-flow boundaries (neutral stream conditions). All no-flow boundaries were defined as zero mass flux boundaries in the transport model and the constant head boundaries were given a background concentration of 0 in MT3DMS. Initially, concentration throughout the domain was set to 0 mg/L, and the upstream cell of the channel (at the constant head boundary) was specified with a concentration of 100 mg/L for 4 hours, followed by 0 mg/L.

Table 2.2 Model Properties

	K (m/d)	Porosity (-)	Thickness (m)	Dispersivity Longitudinal/Transverse (m)
Layer 1	8	0.3	1	0.1 / 0.01
Layer 2-6	1	0.1	1 (per layer)	0.1 / 0.01
Layer 7	0.0005	0.5	5	0.1 / 0.01
Logjam	9028	0.6	1	0.1 / 0.01
Stream	100000	0.9999	1	0.1 / 0.01

To compare the four model configurations, we examined concentration breakthrough curves from nine locations (three points located across three cross-sections or columns of cells) at different locations along the model (Figure 2.4): Site A (X=25 m), Site B (X=29 m), Site C (X=50 m). For the models with a simulated logjam (located at X=27 m, Y=16-17m), Site A is located above the jam and Site B is located below the jam. At each cross-section, Cell 1 is located 1 m below the streambed (at Y=15, Z=2), Cell 2 is located 2 m under the streambed (at Y=15, layer 3), and Cell 3 is located in the stream bank 2 m perpendicular to the stream (at Y=13, layer 1). Temporal moment analysis was performed on the nine breakthrough curves to analyze the movement of the tracer and assess the effect of the logjams at varying flow rates.

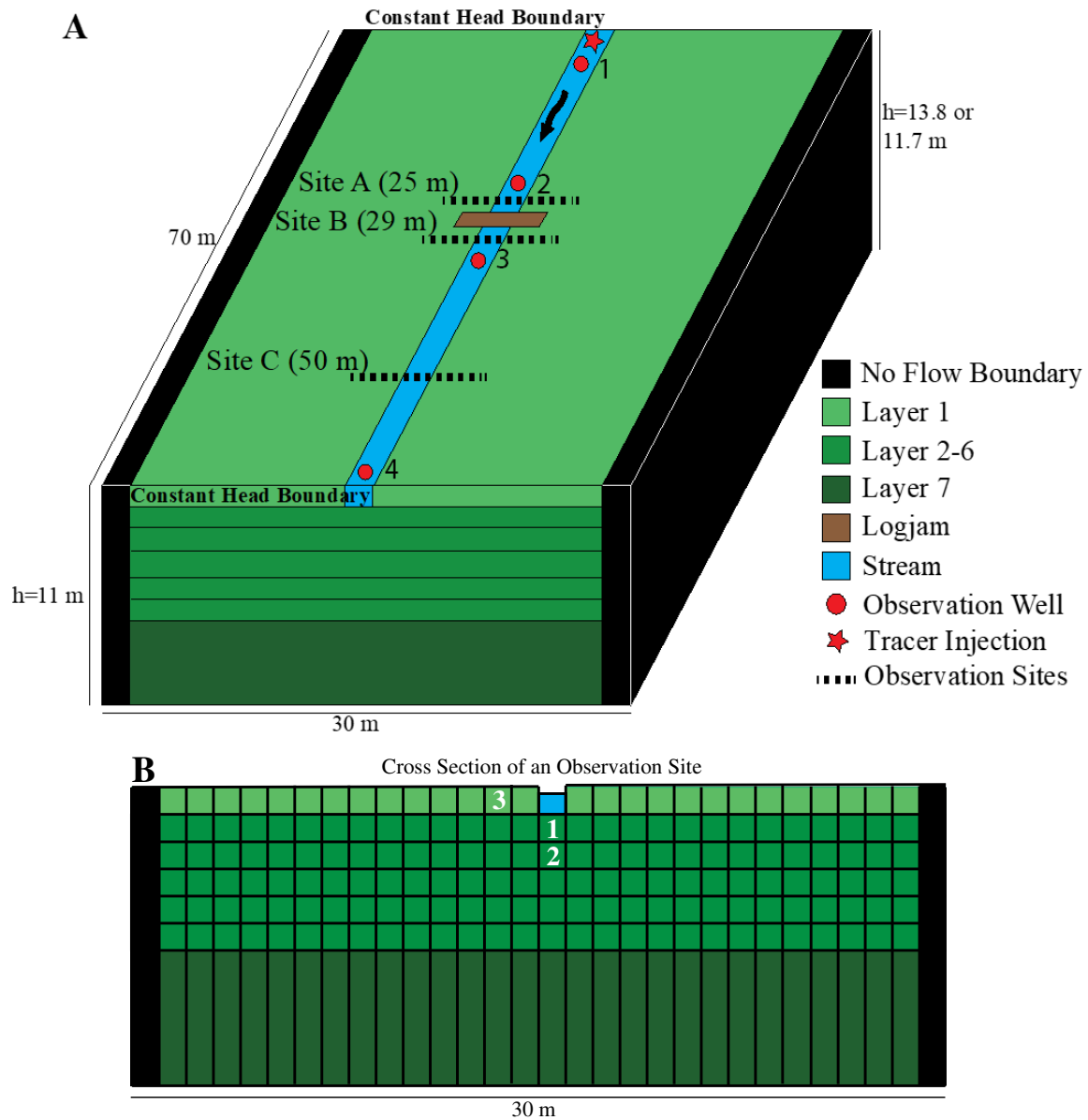


Figure 2.4 (A) Flow and transport model setup, showing the subsurface, the stream, and the logjam (when present, at  $X=27$  m). The top constant head boundary and elevation is 13.8 m for the high-flow and 11.7 m for the low-flow model. Site A ( $X=25$  m), B ( $X=29$  m), and C ( $X=50$  m) are the observation sites where we monitor the three cell concentrations, the locations of which are shown in the cross section (B). Cell 1 is at  $Y = 15$  m and  $Z = 2$  m, cell 2 is at  $Y = 15$  m and  $Z = 3$  m, and cell 3 is at  $Y = 13$  m and  $Z = 1$  m.

## 2.7 Temporal Moments

Solute breakthrough curves can be characterized using the first four moments: mass, mean arrival time, variance, and skew (Gupta and Cvetkovic, 2000; Harvey and Gorelick, 1995). These temporal moments have also been used to characterize breakthrough curves from ER data

(Ward et al., 2010a). To compare temporal trends in observed and modeled breakthrough curves, we analyze the temporal moments of each data set to look for similar behaviors. The  $n^{\text{th}}$  order temporal moment ( $M_n$ ) is calculated by:

$$M_n = \int_0^{\infty} t^n c(t) dt \quad (2.4)$$

$$c = EC * 0.5 \quad (2.5)$$

where  $t$  is time,  $n$  is the order of the moment, and  $c(t)$  is the concentration at time  $t$ . The concentration ( $c$ ) is found by estimating the relationship between total dissolved solids and EC as shown in equation 2.5 (Keller and Frischknecht, 1966). The ER data is averaged for the transect and converted into bulk EC. The zeroth ( $M_0$ ) through the third moment ( $M_3$ ) were calculated to describe the breakthrough curves. To estimate moments, the background concentration was removed from the data before calculations. The zeroth moment ( $\text{mg*s/L}$ ) is the total tracer mass passing the observation point per unit of discharge. To find the total mass passing the observation point, the zeroth moment was multiplied by the average flow. The mean arrival time ( $\bar{t}$ ) of the injected tracer at the point of observation is calculated using:

$$\bar{t} = \frac{M_1}{M_0} \quad (2.6)$$

The variance of the pulse describes the spread of the breakthrough curve and is related to the second, first, and zeroth temporal moments:

$$\sigma^2 = \frac{M_2}{M_0} - \left(\frac{M_1}{M_0}\right)^2 \quad (2.7)$$

The skewness of the data describes asymmetry of the breakthrough curve based on solute retention (Drummond et al., 2012). A more positive skewness ( $\mu_3$ ) value indicates a larger degree of tailing behavior exhibited in the breakthrough curve, and therefore, a higher amount of hyporheic exchange:

$$\mu_3 = \frac{M_3}{M_0} - 3\sigma^2 \frac{M_1}{M_0} - \left(\frac{M_1}{M_0}\right)^3 \quad (2.8)$$

## 2.8 Results: Field Data

The background ER transects show variability in subsurface materials, which is sensitive to rock type, porosity, total dissolved solids, and geologic materials (Figure 2.5A-C, 2.6A-C, and 2.7A-C). The more conductive regions tend to be under the stream and near the surface where the sediments have higher porosity, and less conductive material can be seen deeper into the

subsurface. In the time-lapse inversions, the regions with large increases in bulk conductivity correlate to where the tracer moves through the subsurface. The areas with little to no change in bulk conductivity are where little to no tracer is observed.

### **2.8.1 Control transect**

For all three time periods—June 13-14, July 10-11, and July 28-29—the background bulk conductivity of the control transect (Figure 2.5A, 2.6A, and 2.7A) shows a few zones of low bulk conductivity about a half meter below the surface at about 2 and 10 m along the transect, which likely corresponds to a cobbly layer we observed in the field. The changes in bulk conductivity for the control transect 1 hour after the tracer injection started (Figure 2.5D) show the tracer moving under the stream and into the left bank at a depth from 0.5 to 1 m and along the transect from 4 to 8 m during the tracer injection, regardless of stream flow rate. The percent change in the bulk conductivity is the greatest during the June 13-14 tracer test. The changes in the bulk conductivity for July 10-11 and July 28-29 (Figure 2.6D and 2.7D) have a similar shape and extent as the tracer in the June test, but the percent change in bulk conductivity is lower throughout most of the area. The left bank of the stream has a lower slope angle than the left and is also before a bend in stream, which could favor hyporheic exchange through the left bank. It is difficult to image the tracer once the injection ends for all three tests. The resolution matrices for the control (Figure 2.5J, 2.6J, and 2.7J) show high resolution along the surface about 2 m deep from 0 to 11.5 m, which is where the electrodes start and end.

The fluid conductivity at the control peaks almost immediately after the tracer injection begins for all three tests, plateaus during the injection around 90-100 uS/cm with a slow decrease through the peak, and returns to background almost immediately after the tracer tests end (Figure 2.8A, 2.9A, and 2.10A). There is some fluctuation in the background fluid conductivity values for all tests of approximately +/-3 uS/cm. The average bulk apparent conductivities from the July 10-11 and 28-29 tests across the transect (Figure 2.9A and 2.10A) show a slow increase in bulk conductivity during the tracer plateau instead of a flat constant rate. The slow increase during the tracer plateau can also be seen in the June 13-14 test (Figure 2.8A), but is less distinct. However, there is a greater change in bulk conductivity from background during the June 13-14 tracer test compared to the two tests in July, which plateau at a lower bulk conductivity. The average bulk apparent conductivity does not return to background immediately like the fluid measurements at

any flow rate. There is a small secondary peak after the tracer ends and then a slow return to background on the receding limb. The secondary peak likely came from the slower release of solutes from the logjam site located upstream.

The temporal moment calculations for the control transect (Figure 2.11) were calculated for the fluid conductivity and the average bulk apparent conductivity calculations for all three tracer tests. The masses calculated from the fluid conductivity overestimate the physical mass of salt we injected (Table 2.1) for the June 13-14 and July 28-29 tracer tests. The mean arrival time for the fluid conductivity is 2 hours for June 13-14 and July 10-11, which is the middle of the tracer test as expected. The mean arrival time for the July 28-29 test is 3 hours. The variance and skew for the fluid conductivity are similar across all three tracer tests.

The masses for bulk conductivity are smaller than the calculated mass for the fluid and the injected mass. This is as expected, given the diffusion-based physics of ER (e.g., Singha and Gorelick, 2005). The mean arrival times based on the average bulk apparent conductivity are longer than the fluid and range from 7 to 11 hours, increasing with the lower flows. Given that tracer is moving more slowly through the hyporheic zone and staying in the subsurface after the end of the tracer injection, these numbers seem reasonable. The variance for the bulk conductivity increases through each tracer test. The skew has similarly high values for the June 13-14 and July 28-29 tests, and a lower value for the July 10-11 test.

### **2.8.2 Above the logjam**

The background bulk conductivity of the above-logjam transect (Figure 2.5B, 2.6B, and 2.7B) shows a few zones of low bulk conductivity deeper in the subsurface and some areas of high bulk conductivity right below the stream and near the surface. There is a low bulk conductivity layer about a half-meter down for all three tracer tests that becomes shallower on the right slope, which, again, likely corresponds to the cobbly layer observed in the field. The low bulk conductivity zones may correspond to boulders or bedrock, although we have no data to this depth. The changes in bulk conductivity during the tracer injection (Figure 2.5E, 2.6E, and 2.7E) clearly show the tracer moving through the subsurface of the right bank and partially under the stream at a depth from 0.5 to 2 m and along the transect from 4 to 9 m for all flows. The left bank is steeper and less vegetated. The tracer test from June 13-14 (Figure 2.5E) has a higher percent change in bulk conductivity and also shows the tracer moving at a greater depth

compared to the July 10-11 and July 28-29 tests (Figure 2.6E and 2.7E). The resolution matrix for the above-logjam transect (Figure 2.5K, 2.6K, and 2.7K) shows high resolution along the surface about 2 m deep from 1 to 11 m, which is where the electrodes begin and end.

The fluid conductivity at the above-logjam transect peaks almost instantly after the tracer injection begins, roughly plateaus during the injection (with a slight decrease in peak fluid conductivity throughout plateau), and returns to background soon after the injection ends for all three tracer tests (Figure 2.8B, 2.9B, and 2.10B). Background fluid conductivity values also vary about  $\pm 3$  uS/cm for all three tests, as at the control transect, but stay relatively constant after the tracer test ends. The fluid EC sensor for the above-logjam transect during the June 13-14 test was not in the main flow path, based on the lower peak fluid EC, a longer mean arrival time, and a lower total mass than the other two in-stream monitors. We moved the fluid EC sensor for the other two tracer tests, so that it captured the main flow path. The EC transducer for the above-logjam transect became loose during the July 10-11 test, causing it to be brought to the surface of the stream where it was sometimes underwater and sometimes exposed to the air, which caused notable noise in the measurements. Consequently, temporal moments were not calculated for those data.

The temporal moment calculations (Figure 2.11) show similar values for the fluid conductivity across the different tests. As mentioned above, the fluid conductivity sensor was not placed in the main flow path during the June 13-14 test, so the mass is lower than those calculated for the control and below-logjam transects. The calculated mass at this site is similar to the other two sites for the July 28-29 test, so we successfully fixed the misplacement of the sensor above the logjam. No calculations were made for the July 10-11 test due to the noise in the data, as outlined earlier. The mean arrival time is 2 hours for all the tracer tests, which is in the middle of the injection period, as expected. The variance and skew values estimated from the fluid conductivity are higher for the June 13-14 test than the July 28-29 test.

The mean bulk apparent conductivity values along the transect peaks not long after the tracer injection begins for all three times considered (Figure 2.8B, 2.9B, and 2.10B). During the tracer plateau, the bulk conductivity increases slightly for the June 10-11 and 28-29 tests at the logjam sites, but less than the increase shown at the control. There is a greater change in bulk conductivity during the June 13-14 tracer test from background compared to the two tests in July.

The receding limb of the bulk conductivity slowly returns to background over many hours, exhibiting tailing behavior.

The moment calculations based on the mean bulk apparent conductivity have more variability than the values estimated from the fluid conductivity for the different tracer tests (Figure 2.11). The calculated above-jam masses are consistently smaller than the calculated masses at the control transect for all tests but have a similar magnitude as those calculated for the below-logjam transect. The mean arrival times estimated from the mean bulk apparent conductivity range from 6 to 10 hours, increasing with each tracer test. The mean arrival times are about an hour lower than the control transect but are still close to both the control and below-logjam transect. The variance increases for each tracer test. The skew varies with test, with a higher value for the June 13-14 and July 28-29 tests than the July 10-11 test. This pattern is also seen for the bulk calculations at the below-logjam transect.

### **2.8.3 Below the logjam**

The background bulk conductivity of the below-logjam transect (Figure 2.5C, 2.6C, and 2.7C) shows one main zone of low bulk conductivity in a layer approximately a half-meter deep for all three tracer tests, consistent with the control and above-logjam transects, which likely corresponds to the observed cobbly layer. The changes in bulk conductivity one hour into the tracer injection (Figure 2.5F, 2.6F, and 2.7F) show the tracer moving almost solely under the stream at a depth that appears to be 0.5 to 1 m and along the transect from 4 to 9 m for all three tracer tests. The magnitude of the percent change in bulk conductivity is highest during the June 13-14, while the two later tests show a lower percent change. The July 10-11 test also shows the tracer moving a little deeper in the subsurface toward the left bank, but other than that, the extent of the tracer is similar for all three tests. The difference in bulk conductivity an hour after the tracer injection stopped is subtle in the transects (Figure 2.5I, 2.6I, and 2.7I), but the ER is still picking up the higher fluid conductivity of the tracer after the injection stopped. The resolution matrix for the below-logjam transect (Figure 2.5L, 2.6L, and 2.7L) shows near-perfect resolution along the surface about a half-meter deep from 0 to 11.5 m, where the electrodes start and end, there is a high resolution up to 2 m deep as with the other transects. Similar observations can be made of the resolution transects from July 10 and July 28 tests (Figure 2.9, 2.6, and 2.7).

The fluid conductivity at the below-logjam transect peaks almost immediately after the tracer injection begins, roughly plateaus at 90-100 uS/cm during the injection with a slow decline in EC, and sharply returns to background soon after the injection ends for all three tests (Figure 2.8, 2.9, and 2.10). The background fluid conductivity fluctuates approximately +/-3 uS/cm for all three tests. The temporal moment calculations for the below-logjam transect (Figure 2.11) are very similar to the values for the above-logjam transect. The mass calculated from the fluid conductivity is large and overestimates the injected mass for the June 13-14 and July 28-29 tests due to the assumptions from the bulk conductivity to TDS conversion. The mean arrival times are all 2 hours as expected, which is the middle of the injection period. The variance and skew for the fluid calculations are highest for the first test in June and decrease in the tests in July.

The mean bulk apparent conductivity values across the transect rapidly peak soon after the start of the tracer injection, plateau with some fluctuations during the tracer, and then drop in bulk conductivity after the tracer ends but do not return to background values (Figure 2.8, 2.9, and 2.10). There is a larger change in bulk conductivity from background during the June 13-14 tracer test than the two tests from July. The drop in bulk conductivity after the tracer ends is more gradual during the July 28-29 test, but this is likely due to gaps in data caused by passing storms that day. The July 10-11 and July 28-29 tests have a gradual increase in bulk apparent conductivity during the plateau during the tracer injection. These increases also occur at the control but are lower.

The masses calculated for the mean bulk apparent conductivity are low, as expected. As mentioned previously, the mass from the mean bulk apparent conductivity is likely still an overestimate of the mass actually observed in the transects due to using the stream discharge as the flow through the subsurface. The mean arrival times range from 5 to 9 hours. The variance for the bulk conductivity increases in each consecutive tracer test. The skew, however, does not demonstrate this pattern. The highest value (also the highest skew out of all the calculations) occurs during the July 28-29 test and the lowest is from the July 10-11 test. The skew values for June 13-14 and June 10-11 are very similar to the above-logjam transect skews. The calculated skew for the last tracer test in July is substantially larger than the control and above-logjam transect values or the skew values for the other two tracer tests.

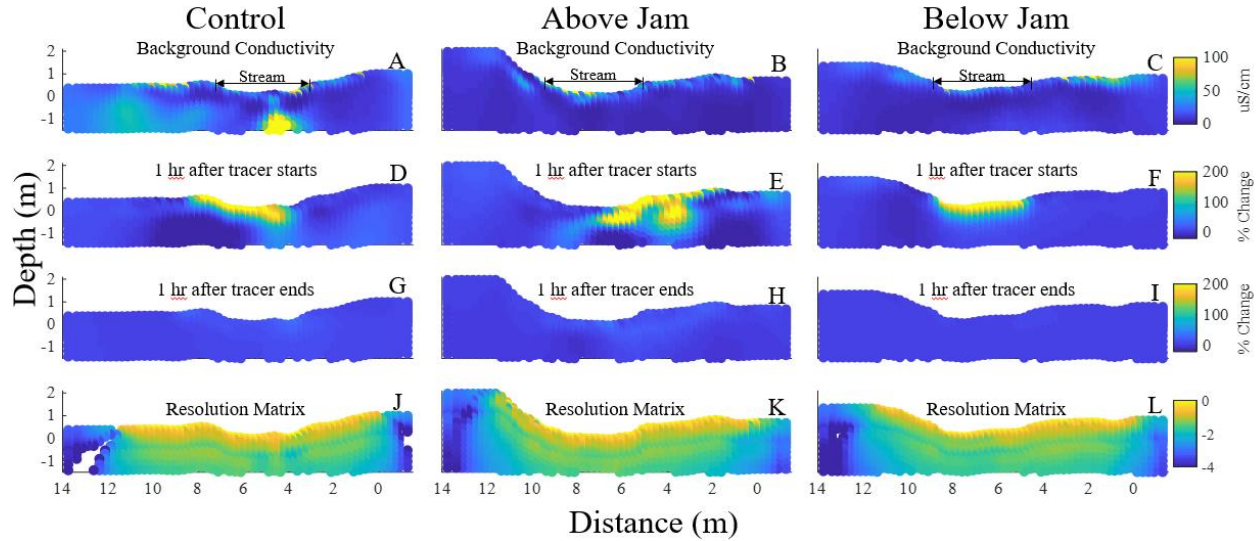


Figure 2.5 Data from the three transects, oriented looking downstream, from the June 13-14 tracer test. A-C: background bulk conductivity along the three ER transects (background fluid conductivity of 23.2 uS/cm). D-F: changes in bulk conductivity 1 hr into the tracer injection. G-I: changes in bulk conductivity 1 hr after the tracer injection ended. J-L: resolution matrix of the three transects ( $\log_{10}(\text{diagonal resolution matrix})$ ). Pixels close to 0 in  $\log_{10}$  space have perfect resolution. The more negative a pixel in  $\log$  space, the less perfect the resolution.

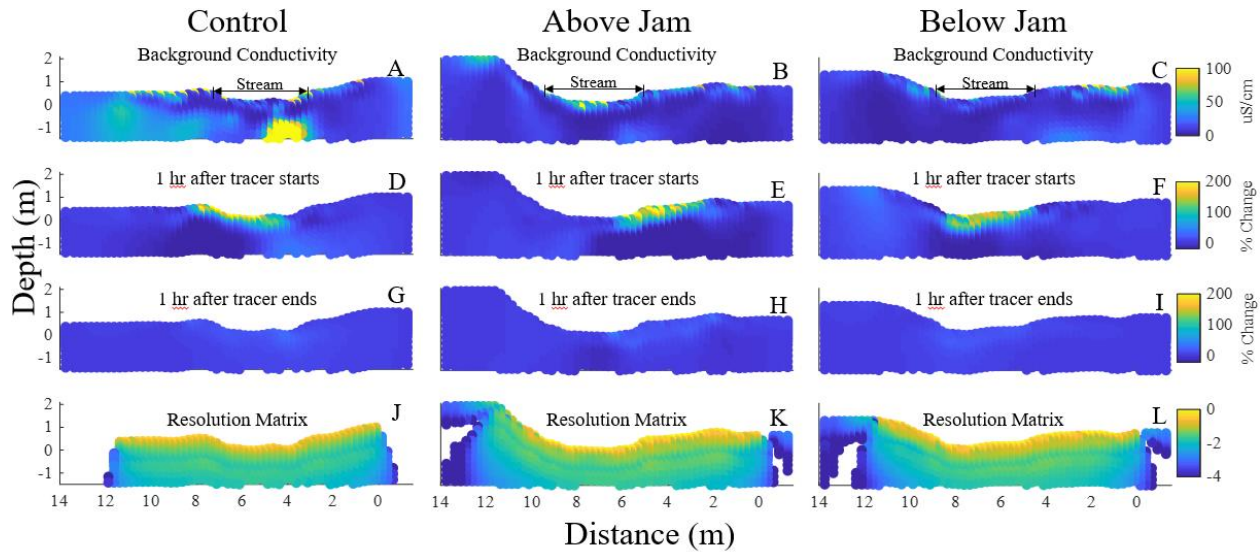


Figure 2.6 Data from the three transects, oriented looking downstream, from the July 10-11 tracer test. A-C: background bulk conductivity along the three ER transects (background fluid conductivity of 29.5 uS/cm). D-F: changes in bulk conductivity 1 hr into the tracer injection. G-I: changes in bulk conductivity 1 hr after the tracer injection ended. J-L: resolution matrix of the three transects ( $\log_{10}(\text{diagonal resolution matrix})$ ).

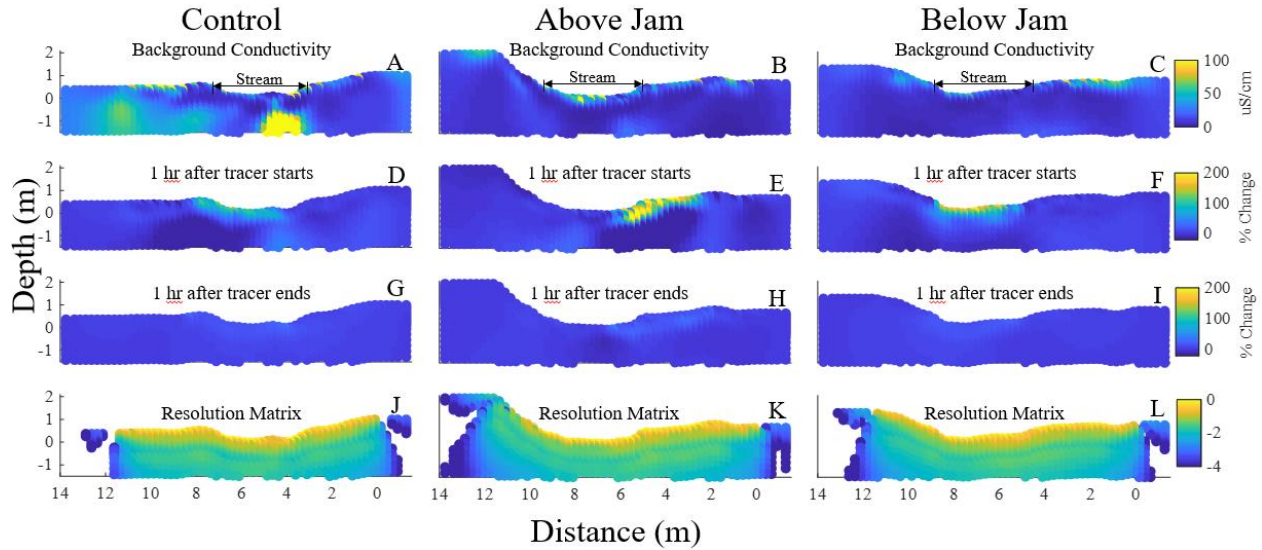


Figure 2.7 Data from the three transects, oriented looking downstream, from the July 28-29 tracer test. A-C: background bulk conductivity along the three ER transects (background fluid conductivity of 35.0 uS/cm). D-F: changes in bulk conductivity 1 hr into the tracer injection. G-I: changes in bulk conductivity 1 hr after the tracer injection ended. J-L: resolution matrix of the three transects ( $\log_{10}(\text{diagonal resolution matrix})$ ).

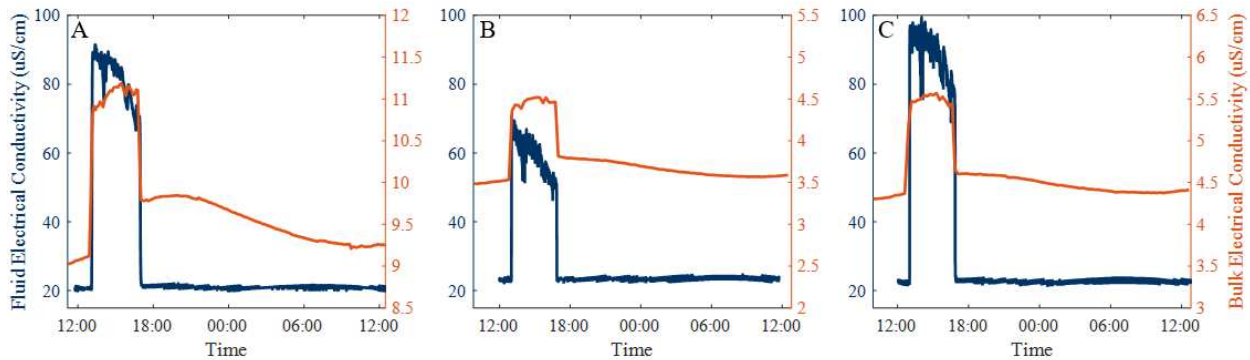


Figure 2.8 Fluid and mean bulk apparent conductivity from the June 13-14 tracer test for the (A) control, (B) above-logjam, and (C) below-logjam sites.

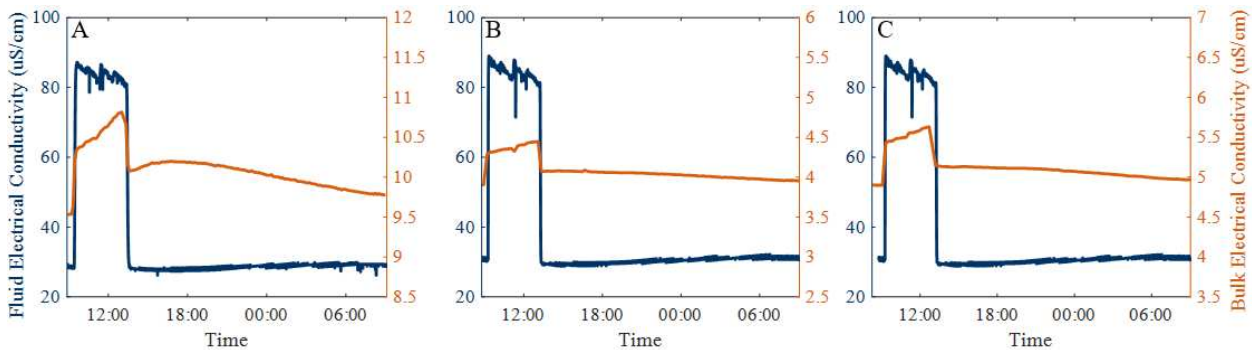


Figure 2.9 Fluid and mean bulk apparent conductivity from the July 10-11 tracer test for the (A) control, (B) above-logjam, and (C) below-logjam sites.

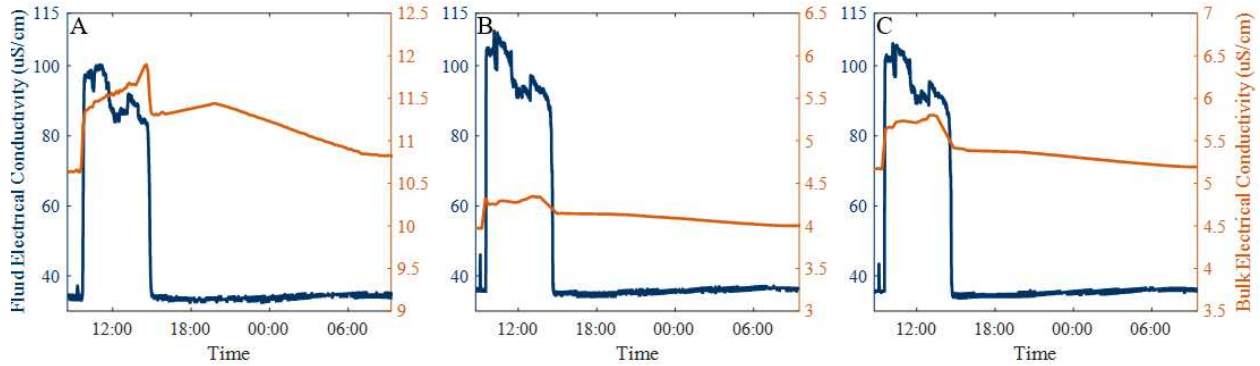


Figure 2.10 Fluid and mean bulk apparent conductivity from the July 28-29 tracer test for the (A) control, (B) above-logjam, and (C) below-logjam sites.

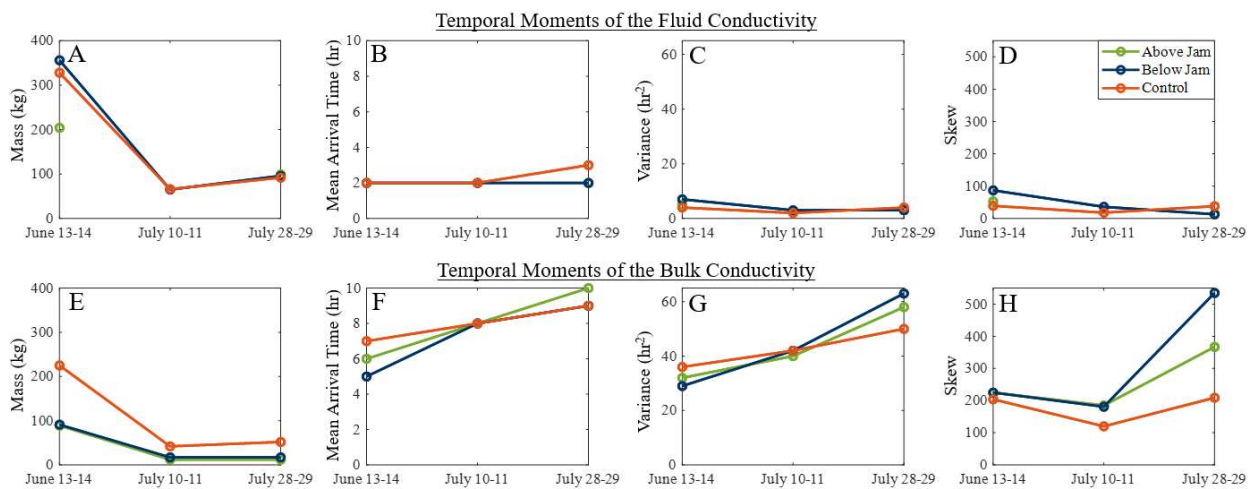


Figure 2.11 Temporal moments (mass, mean arrival time, variance, and skew) estimated from the mean fluid apparent conductivity (A-D) and bulk apparent conductivity (E-H) through time.

## 2.9 Results: Numerical Modeling

Here, we describe the results of our four model configurations: a tracer test in a synthetic stream 1) without a logjam at high flow ( $Q=0.05$  cms), 2) with a logjam at high flow ( $Q=0.05$  cms), 3) without a logjam at low flow ( $Q=0.01$  cms), and 4) with a logjam at low flow ( $Q=0.01$  cms). We look at breakthrough curves from three locations at Site A ( $X=25$  m), Site B ( $X=29$  m), and Site C ( $X=50$  m), at three cells in each site, where cell 1 is 1 m below the stream ( $Y=15$  m,  $Z=2$  m), cell 2 is 2 m below the stream ( $Y=15$  m,  $Z=3$  m), and cell 3 is 2 m lateral to the stream ( $Y=13$  m,  $Z=1$  m) (Figure 2.4B). In the logjam systems, the logjam is present at  $X=27$  m and  $Y=14-16$  m. The temporal moments were calculated for each cell at the three sites (A, B, and C) (Figure 2.14).

### **2.9.1 No-logjam, Low-flow**

The breakthrough curve 1 m below the stream (at  $Y=15$  m,  $Z=2$  m) for the no-logjam, low-flow model has a similar shape and magnitude at sites A, B, and C along the stream (Figure 2.12A-C). Concentration increases rapidly after the start of the tracer, although it has a more gradual rising limb than the high-flow models. It peaks at a concentration of 59, 57, and 46 mg/L 1 m below the stream at the three sites, respectively. The receding limb decreases rapidly after the end of the tracer, but more gradually than the high flow models. The mass, mean arrival time, variance, and skew are approximately the same 1 m below the stream for all three sites (Figure 2.14).

The concentrations 2 m below the stream (at  $Y=15$  m,  $Z=3$  m) and 2 m lateral to the stream (at  $Y=13$  m,  $Z=1$  m) are very similar across space in this model, as little to no concentration was detected in any of the locations (Figure 2.12D-F). Temporal moments were not calculated 2 m below the stream, because the concentration in the cell was never greater than 0.01 mg/L. For 2 m below the stream, a small peak was observed at 0.06 mg/L and the concentration remained below this value throughout the rest of the monitoring period. Observed mass, mean arrival time, variance, and skew values 2 m lateral to the stream increased from Site A to B to C (Figure 2.14).

### **2.9.2 No-logjam, High-flow**

The breakthrough curves for the high-flow, no-jam model from a depth of 1 m below the channel (at  $Y=15$  m,  $Z=2$  m) look similar for the three sites, or distances along the stream. In all locations 1 m below the stream, the rising limb peaks rapidly after the start of the tracer test and reaches a peak concentration of approximately 98 mg/L (Figure 2.12A-C). The concentration drops quickly 1 m below the stream after the tracer ends and returns to background concentration (0 mg/L) after some tailing in the receding limb. The mass, mean arrival time, variance, and skew remain relatively consistent at all three sites for cell 1 (Figure 2.14).

The breakthrough curves 2 m below the stream (at  $Y=15$  m,  $Z=3$  m) also show similar behavior along the reach (Figure 2.12D-F). The concentration remains at or close to zero throughout the duration of the tracer test, meaning very little of the tracer reached a depth 2 m below the stream. The upper temporal moments were not calculated for the cell 2 m below the stream at any of the three sites since the concentration was never greater than 0.01 mg/L for the

duration of the monitoring period. The total mass observed in the cell 2 m below the stream is more than an order of magnitude lower than the masses observed 1 m below the stream and 2 m lateral to the stream at all observation sites, so little to none of the tracer extends 2 m below the stream.

The breakthrough curves at a depth of 1 m (at  $Y=13$  m,  $Z=1$  m) also show similar behavior along the channel (Figure 2.12G-I): a trace amount of the tracer is detected after the start of the test and slowly decreases throughout the remaining monitoring period. The no-logjam, high-flow model shows few differences in the extent and magnitude of the concentration in the three cells regardless of site. The mass, mean arrival time and variance remain relatively consistent at all three sites (Figure 2.14). The skew increases downgradient from Site A to B to C for the cell 2 m lateral to the stream, as well.

### **2.9.3 Logjam, Low-flow**

The breakthrough curve 1 m below the stream for the logjam, low-flow model is similar at all three locations in the model explored and has a similar shape and magnitude to the no-jam, low-flow model (Figure 2.12A-C). The concentration peaks soon after the start of the tracer test at 54, 49, and 42 mg/L for the three sites, respectively. The total mass 1 m below the stream was consistent at every observation location (Figure 2.14). The mean arrival time was similar 1 m below the stream for Sites A and C, but was a little more than twice as long for Site B. The skew and variance increased at 1 m below the stream from Sites A to B, but decreased from Sites B to C. The skew was four orders of magnitude higher 1 m below the stream at Site B and only slightly higher at Site C in the logjam, low-flow model compared to the no-logjam, low-flow model.

The concentration at 2 m below the stream (at  $Y=15$  m,  $Z=3$  m) changes with the three locations (Figure 2.12D-F). For Site A, it peaks in concentration at 2 mg/L soon after the start of the tracer test, but it has a gradual rising limb. After the tracer ends, it slowly and steadily decreases through the remaining monitoring period, but never returns to background concentration. Site B 2 m below the stream has a steady increase in concentration starting at the beginning of the tracer test. It peaks a long time after the tracer ends around 0.7 mg/L. There is little to no tracer observed 2 m below the stream at Site C. Temporal moments were not calculated for 2 m below the stream at Site C (Figure 2.14) because the total mass was so low and the concentration in the cell was never greater than 0.011 mg/L. The total mass observed was

similar in magnitude from Sites A to B to C. This was the same pattern observed 2 m below the stream for the logjam, high-flow model. The skews for 2 m below the stream increase from Site A to Site B and are larger than those in the logjam, high-flow model.

The cell located 2 m lateral to the stream (at  $Y=13$  m,  $Z=1$  m) also shows substantial differences in concentration at the different locations for this model configuration (Figure 2.12G-I). At Site A, the breakthrough curve peaks at 5 mg/L soon after the start of the tracer test with a gradual rising limb. The receding limb decreases slowly for the remaining monitoring period although at a faster rate than 2 m below the stream at Site A. The concentration at Site B location increases slowly after the start of the tracer test and does not peak until long after the tracer test ends at 2 mg/L. Site C concentration for 2 m lateral to the stream is low with only a slight peak at 0.05 mg/L after the start of the tracer, and it remains at or close to zero for most of the monitoring period. In the cell 2 m lateral to the stream, the total mass observed was similar in magnitude from Sites A to B but decreased at Site C (Figure 2.14). This was the same pattern observed 2 m lateral to the stream for the logjam, high-flow model. The skews 2 m lateral to the stream increase from Site A to Site B and are larger than those in the logjam, high-flow model. The skew value 2 m lateral to the stream at Site C was calculated as negative, but this is because of the secondary peak experienced in this cell (Figure 2.13). As with the logjam, high-flow model, tracer was pushed deeper into the subsurface at the logjam and traveled downgradient at a slower velocity than the particles in the stream. This caused negative values in the moment calculations and produced a negative skew even though this shows the higher amount of tailing occurring in this model compared to the no-logjam models.

#### **2.9.4 Logjam, High-flow**

The breakthrough curve 1 m below the stream (at  $Y=15$  m,  $Z=2$  m) for the high-flow, logjam model behaves similarly at the three monitoring sites (Figure 2.12A-C): there is a plateau in concentration near 95 mg/L at all three sites after the tracer begins. The concentration drops quickly after the end of the tracer and returns to background concentrations (0 mg/L). Cell 1, 1 m below the stream, has approximately the same mass and mean arrival time at the three locations. The variance and skew 1 m below the stream increase downgradient from Site A to B, but the skew decreases at Site C (Figure 2.14).

The breakthrough curve 2 m below the stream (at  $Y=15$  m,  $Z=3$  m) changes drastically with distance downstream in the model (Figure 2.12D-F). At Site A ( $X=25$  m), the concentration

2 m below the stream peaks at 7 mg/L soon after the start of the tracer, and slowly decreases on the receding limb. The concentration in this cell never returns to background before the end of the monitoring period. The concentration 2 m below the stream at Site B ( $X=29$  m) shows a slow increase in concentration after the start of the tracer and a peak of 3 mg/L. The receding limb decreases slowly through the remaining monitoring period, but never returns to background concentrations. The breakthrough curve at Site C ( $X=50$  m) 2 m below the stream shows a small concentration after the start of the tracer and a slow decrease afterward. The highest concentration at this cell is 0.2 mg/L. The mass 2 m below the stream is similar between Sites A and B but decreases at Site C (Figure 2.14). The skew 2 m below the stream increases from Sites A to B, and has a negative skew value at Site C. This is because cell 2 has a secondary peak in concentration (Figure 2.13).

The breakthrough curves from 2 m lateral to the stream (at  $Y=13$  m,  $Z=1$  m) also change notably at the different sites (Figure 2.12G-I). Site A increases rapidly after the start of the tracer test and peaks at 17 mg/L. After the tracer ends, the receding limb decreases rapidly and then more slowly over time. It does not return to background concentrations by the end of the monitoring period. The cell located 2 m lateral to the stream at Site B peaks at 8 mg/L soon after the start of the tracer test, but with a more gradual rising limb compared to Site A. The receding limb decreases and never returns to background concentrations by the end of the monitoring period. At the logjam between sites A and B, the tracer is pushed deeper into the subsurface as well as laterally away from the stream. Site C is far enough downgradient that it experiences a second peak as a result. The secondary peak creates negative values in the moment calculations and results in a negative skew if the rising limb of the secondary peak is larger than the first. Site B is close enough to Site A that it does not experience a secondary peak and instead the increased concentration just contributes to the receding limb. The concentration 2 m lateral to the stream at Site C peaks at 0.6 mg/L soon after the start of the tracer test. It slowly decreases through the remaining time monitoring period, but never exceeds trace concentrations. The mass 2 m lateral to the stream is similar between Site A and B but decreases at Site C (Figure 2.14). The mass 2 m lateral to the stream is similar between Site A and B but decreases at Site C. The mean arrival time, variance, and skew increase 2 m lateral to the stream from Site A to B to C. Although the skew is positive at Site C 2 m lateral to the stream, it is not as large as it might be because of the second peak (Figure 2.13).

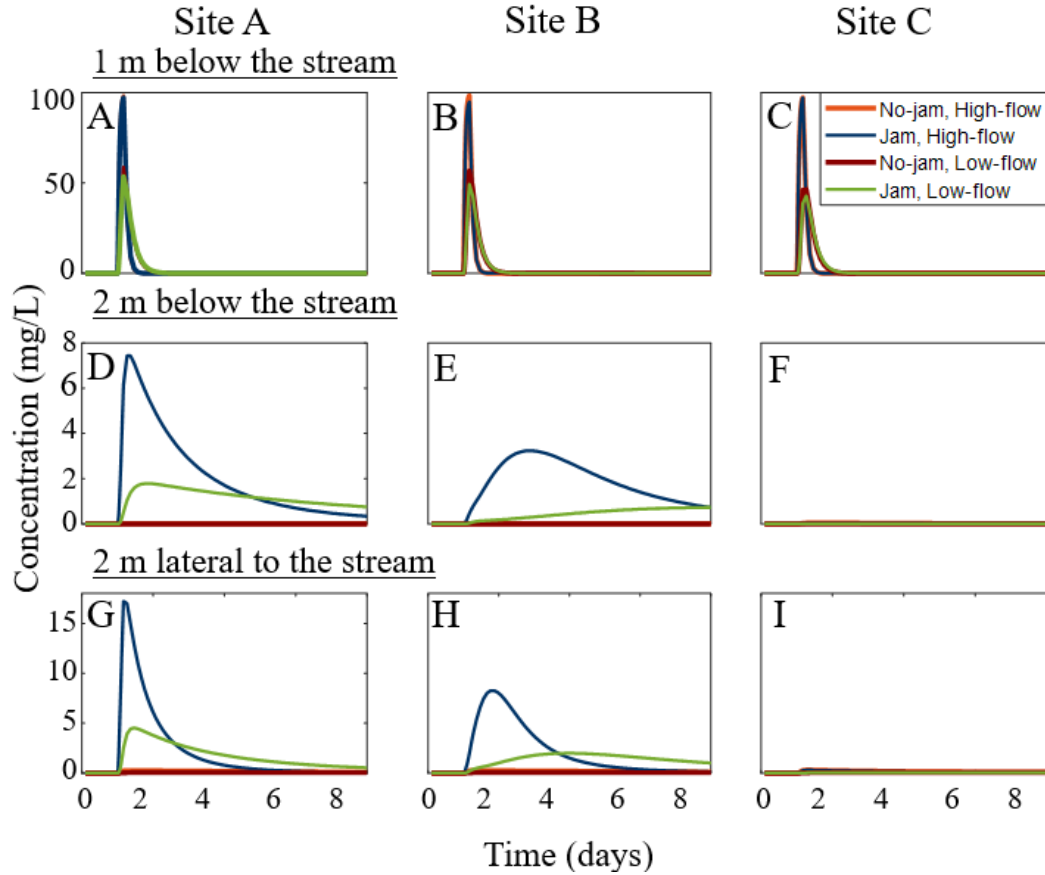


Figure 2.12 Concentration plots (mg/L) from Modflow and MT3D for the three sites (A, B, C) from the four model configurations. Concentrations 1 m below the stream ( $Y=15$  m,  $Z=2$  m) are plotted in A-C. Concentrations 2 m below the stream ( $Y=15$  m,  $Z=3$  m) are plotted in D-F. Concentrations 2 m lateral to the stream ( $Y=13$  m,  $Z=1$  m) are plotted in G-I. Only the first 8 days of the 100-day monitoring period are shown.

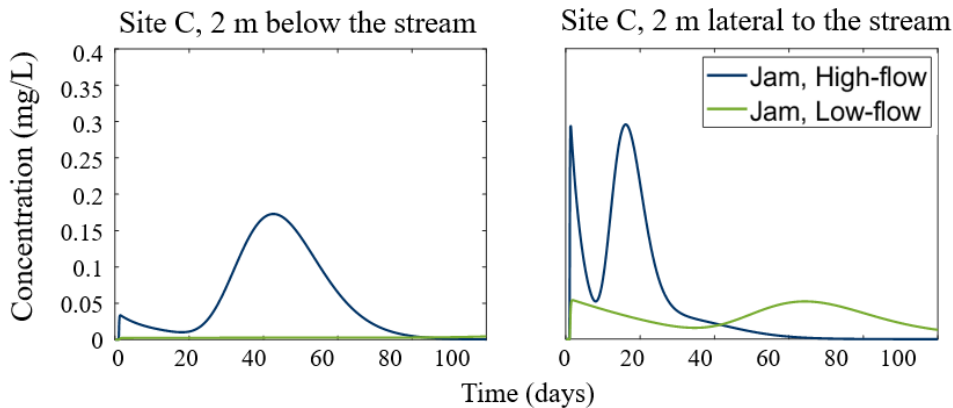


Figure 2.13 Comparison of the concentration 2 m below the stream and 2 m lateral to the stream for the logjam, high-flow model and the logjam, low-flow model at Site C ( $X = 50$  m), showing a secondary peak. The cell 2 m below the stream for the logjam, low-flow model shows that the concentration in that cell remained close to zero for the entire period.

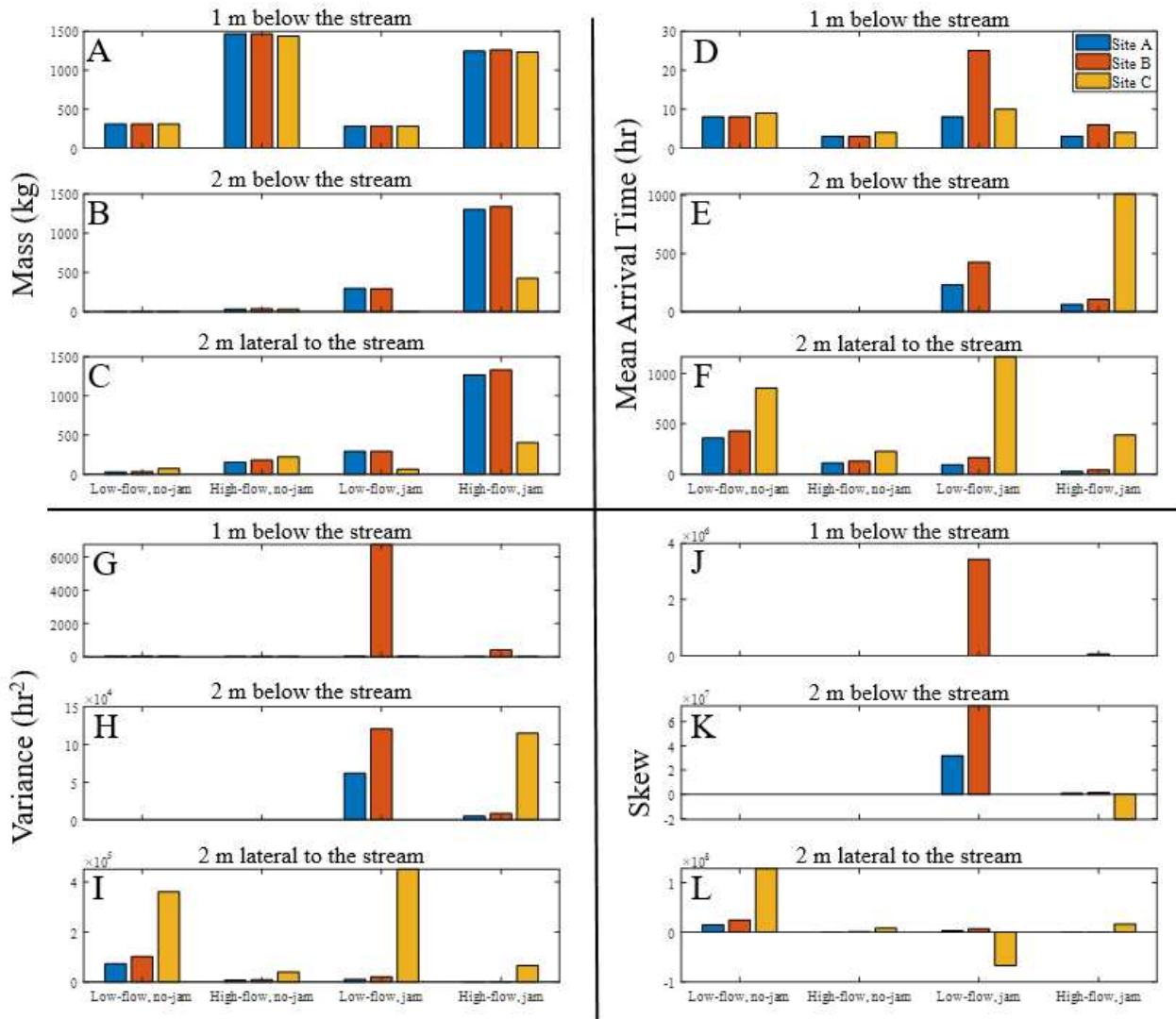


Figure 2.14 Bar plots of the temporal moments for the model. Mass (A-C), mean arrival time (D-F), variance (G-I), and skew (J-L) values from the four model configurations for all three sites 1 m below the stream (A, D, G, and J), 2 m below the stream (B, E, H, and K), and 2 m lateral to the stream (C, F, I, and L).

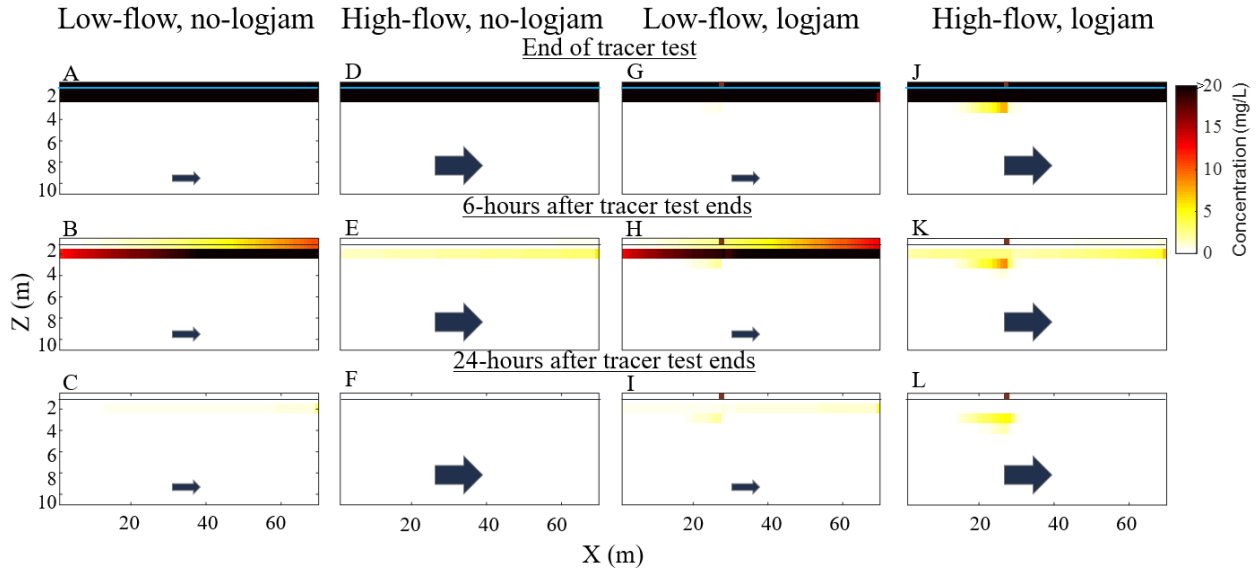


Figure 2.15 Concentration in the cross section along the stream ( $Y=15$  m) of the four model configurations: (A-C) low-flow, no-logjam, (D-F) high-flow, no-logjam, (G-I) low-flow, logjam, and (J-L) high-flow, logjam. The blue line indicates the bottom of the streambed, the small brown box at  $X=27$  m represents the location of the logjam, and the arrows correlate with the flow rate (small=low flow, large= high flow). The first row is at the end of the tracer test, the second row is 6 hours after the tracer test ends, and the last row is 24 hours after the tracer test ends.

## 2.10 Discussion

### 2.10.1 Comparison of logjam and control transects in the field

While we did our best to create a natural experiment in which the primary difference between sites was the presence or absence of a logjam, this is a natural stream with substantial spatial heterogeneity. Consequently, there are differences in alluvial sediment width, depth, porosity, and permeability between the logjam and control sites that will influence the results in ways that are difficult for us to quantify and compare. The control site is also downstream of the logjam site, which was the only feasible option for these experiments.

Near-stream vegetation and streambank slope likely control the movement of tracer in the field. For example, the tracer at the control transect moves underneath the streambed and into the left bank (Figure 2.5D, 2.6D, and 2.7D), potentially due to the lower slope and high density of vegetation on the left bank. The vegetation could be pulling from the stream as well as creating more porosity in the underlying material, which would cause HEF to favor that bank. Similarly, the tracer at the above-logjam transect moves mostly through the right bank of the stream (Figure 2.5E, 2.6E, and 2.7E), which was highly vegetated, had a lower slope, and had

standing water during high flows. The standing water suggests that the water table is near the surface, allowing an easier exchange of water. The steepness of the left bank could also indicate shallower bedrock and therefore lower hydraulic conductivity of the subsurface material.

The tracer at the below-logjam transect is solely under the stream with little exchange occurring in the banks of the stream (Figure 2.5F, 2.6F, and 2.7F). While the site characteristics are similar at the below-logjam and above-logjam transect, there is no logjam-induced head gradient nor pooling, so no driving force to push water to either side.

The observed mass based on the mean bulk apparent conductivity calculations at the control transect is consistently larger than the logjam transects (Figures 2.8-10; Table 4). This is likely because the tracer was more dispersed by the time it reached the downstream control transect, and the ER is more sensitive to a dispersed target than to high, focused concentrations (Bethune et al., 2015), so that the estimates of tracer mass will be higher at the control. Notably, the masses calculated from the fluid conductivity overestimate the physical mass of injected salt (Table 2.1) for the June 13-14 and July 28-29 tracer tests. This is likely due to compounding errors from the assumptions made in our calculations, including the assumption that the tracer was fully mixed and that the conversion factor for fluid conductivity to TDS was exactly known.

The higher-order moments also provide insight into the hydrologic system. The mean arrival times based on the mean bulk apparent conductivity for the control transect are consistently an hour to three hours longer than the logjam sites. Based on the stream discharge, it takes approximately 10 minutes for the tracer to reach the control from the injection point in the stream, and transport through the aquifer would obviously be slower. The temporal variance tends to be slightly larger for the control transect than at the logjam transects, which means larger dispersion is observed at the control compared to the logjam sites. The downstream position of the control site would require more time for the dispersion of the tracer compared to the upstream logjam sites closer to the injection. The skew values are higher for both logjam sites compared to the control, which is interpreted as higher retention; the logjam sites show a much slower return to background when compared to the rapid decrease seen in the control. For two out of the three tracer tests, the skew and therefore the interpreted retention at the above- and below-logjam were very similar. The last tracer test showed a high amount of tailing below the logjam not seen above.

While we would expect reaches with logjams to have higher retention than those without logjams, the lower skew at the control transect might be surprising given that this location is below the logjam transects. However, the mean bulk apparent conductivity at the control transect (Figure 2.8A, 2.9A, and 2.10A) shows a secondary peak after the tracer ends for all three tracer tests that is not observed at the logjam sites. The secondary peak likely causes the skew values to be lower at the control site than would otherwise be seen, because the rising limb of the second peak creates negative moments in the calculation. This secondary peak is likely an effect of the control transect being downstream of the logjam site. The slow movement of the tracer through the subsurface from the logjam site likely causes the secondary peak in the bulk conductivity. There are no discernable changes between the fluid EC measurements at all the sites and the secondary peaks in the control bulk conductivity so it is reasonable to assume this is solely a hyporheic process.

### **2.10.2 Comparison of high vs low flows in the field**

Streamflow also controls the estimated moments in the field (Table 2.4). The mass calculated from both the fluid and bulk conductivity at all three sites decreased from the high flow (June 13) to the low flows (July 10 and 28), which corresponds to the actual injected mass (Table 2.1). More mass was injected during the higher flow to create a similar increase in in-stream fluid conductivity. The increased injection mass is visible as larger percent changes in the ER inversions (Figure 2.5, 2.6, and 2.7).

The mean arrival times are longer at each transect for the lower flows compared to the higher flow, which is expected. Similarly, the temporal variance increases with a lower flow. This could be due to more zones of slower moving pools, eddies, or dead zones, which would allow for more dispersion and a larger spread of the breakthrough curves. However, there is not a distinct pattern for the skew value with varying flows. The July 10-11 test had the lowest skew values, but it had a similar flow to the July 28-29 test, which has the highest skew values. One complication in our analyses is that there were thunderstorms throughout the day on July 28, including heavy rain and lightning; the former undoubtedly altered the fluid and bulk conductivity and the latter forced us to turn off our ER monitoring. Consequently, we lost data during the tracer injection and within the few hours after the tracer stopped. The biggest gap in data is between 15:53 and 19:12; the end of this data gap is where the large secondary peak in

the control occurs. While both the July 10-11 and July 28-29 tests had similar flow ( $Q = 0.17$  and  $0.18$  cms), there is a notable difference in the moment calculations, specifically the skew. However, if the rain increased the bulk electrical conductivities, this would give us an overestimated skew. A higher moisture content in the ground could increase the background bulk conductivity therefore exaggerating tailing and the calculated skew by measuring higher bulk conductivity than the original background.

The larger change in bulk conductivity and deeper flow paths suggest that higher flows increase the extent of HEF and the amount of stream water entering the hyporheic zone but do not necessarily increase the time water particles spend in the subsurface. The inconsistent skew values for the low flows and the longer mean arrival times could mean that water moves through the hyporheic more slowly during lower flows, but the extent of HEF is smaller compared to high flows.

### **2.10.3 Insights from numerical modeling**

Two inferences can be made from our numerical models: 1) logjams increase the extent and amount of the tracer movement into the subsurface and 2) lower flow increases tailing. In terms of logjams increasing the extent and amount of HEF, the model results show the tracer reaching a greater subsurface depth (Figure 2.15) and larger calculated skew values from the two models with logjams (Figure 2.14). There was a greater total mass and more tailing behavior (Figure 2.12) observed in 2 m below the stream and 2 m lateral to the stream, the cells farthest from the stream, for the logjam models compared to their no-logjam counterpart models. These model results supports our expectations and findings from the field for the impacts of logjams. The model also allows us to see the exact behavior of the tracer in these systems, so we know there is a large flux of the tracer into the subsurface above the logjam and that some of the tracer stays in the hyporheic zone until the model boundary (Figure 2.15). This pattern was similar in the field as well: the skew values for all three tracer tests at the two logjam sites were larger than the control's skew. Deeper flow paths in the above logjam transect (Figure 2.5E) correspond to the deeper movement of the tracer in the logjam, high-flow model (2 m below the stream, Site A) compared to the low-flow, logjam model, which did not have detectible tracer in that cell (Figure 2.5, 2.6, and 2.7). The tracer remaining in the hyporheic zone for the logjam models explains the secondary peak at the control site in the field as well.

The observed secondary peak at the control site in the field and at Site C in the logjam models is one of the most interesting similarities between the field measurements and the numerical modeling. The bulk conductivity at the control transect had a secondary peak a few hours after the end of the injection period for all three tracer tests (Figure 2.8A, 2.9A, and 2.10A). Both of the models with a logjam present also had a secondary peak at Site C (Figure 2.13), which is downstream of the logjam. Since this secondary peak was not observed in the no-logjam models, it can be assumed that the secondary peak is a direct effect of the logjam. This could mean that the secondary peak at the control was from tracer remaining in the hyporheic zone from the logjam, as in the model. These secondary peaks also explain why the skew value is lower at the control site and at Site C compared to the upstream sites. The skew values 1 m below the stream at Site C (Figure 2.14) are much smaller than the values 1 m below the stream at Site B for both of the logjam models despite Site C being downstream. The control similarly has lower skew values compared to the logjam sites, and both of these are likely due to the secondary peak creating negative moments in the calculation. This would decrease the skew values as we observe in both the field and model results.

For the second inference, the model results indicate higher retention times in the low flow models compared to the high flow models. The low-flow, logjam model exhibit this increases in tailing through the consistently higher skew values in comparison to the high-flow, logjam model in every cell at all sites except where concentrations were too low for moment calculations or the second peak caused a negative skew value (2 m lateral to the stream, Site C). While the model shows that that lower flow increases the tailing compared to the high flow, this was not observed in the field measurements. The inconsistent skew values for two low flow tests in July are less conclusive about the effect of flows on retention times. More field data and models are required to characterize this relationship adequately. There likely is not a linear relationship with either residence times or flow.

## **2.11 Conclusions**

Both our field measurements and numerical models support the conclusion that logjams increase HEF. Our model provides an idealized look at our stream system, however, we see similar behaviors between the model and our field measurements. Longer tailing, as quantified by the temporal moment skew, was observed in both the field measurements and modeling

results for reaches with logjams compared to those without. The numerical models built for this study show that a lower flow increases the tailing associated with HEF, but not all of the field data support this, perhaps in part due to thunderstorms impacting one tracer test. Therefore, conclusions on the effect of flow on increased tailing are inconclusive in the field, although it appears that lower flows increase the time water spends in the hyporheic zone based on our models. Our results suggest that higher flows may increase the extent and amount of hyporheic exchange. The detection of the tracer to a 3 m depth in the logjam, high-flow model compared to a 2 m depth in the low-flow, logjam model, as well as the larger HEF extent observed during the high flow at the above logjam transect (Figure 2.5E) compared to the low flows (Figure 2.6E and 2.7E) in the field, supports the idea that higher flows increase the extent and amount of HEF. Lower flows have a smaller extent of HEF and they decrease the flow in the hyporheic zone, possibly resulting in longer residence times.

ER allows us to estimate approximately changes in hyporheic extent. We observe the tracer in the subsurface long after the fluid conductivity of the stream returns to background. The bulk conductivity and fluid conductivity comparison plots (Figure 2.8, 2.9, and 2.10) demonstrate the ability of ER to monitor tracer in the hyporheic zone. The transect imaging (Figure 2.5, 2.6, and 2.7) also provides valuable information on the relative extent and flowpaths of HEF. ER provides a noninvasive improvement over point measurements in stream.

These findings can be used to advance stream restoration and conservation efforts providing a foundation for placing wood or engineered logjams into streams and suggesting ER as a long-term monitoring method. River management operations, such as adding large wood in streams, often involve strategies to offset negative impacts that were manifested from controlling and engineering stream systems and altering land use (Kail et al., 2007). Currently, many of the river management and restoration practices that incorporate large wood placement use few quantitative or predictive methods for implementation. This research aims to advance the predictive and quantitative basis for using large wood and logjams for restoration by characterizing the relationship between logjams and hyporheic exchange rates. Future work with this research involves characterizing more complex logjam systems, logjam spacing, and the effect on HEF, which will also advance engineered logjams. ER methods can be time intensive and require a high initial cost so it would not be an ideal fit for universal long-term monitoring

method for restoration efforts. However, it can be used to further research in restoration efforts and has been used to look at changes in hyporheic processes in other stream restoration structures (Toran et al., 2012; Toran et al., 2013). The results from the ER measurements could also provide a basis for more practical long-term monitoring methods that could be used for restoration project such as measuring stream temperature and head drops across structures like logjams.

## REFERENCES CITED

- Allan, J. D. (2004). Landscapes and Riverscapes : The Influence of Land Use on Stream Ecosystems. *Annual Review of Ecology, Evolution, and Systematics*.  
<https://doi.org/10.1146/annurev.ecolsys.35.120202.110122>
- Anderson, J. K., Wondzell, S. M., Gooseff, M. N., & Haggerty, R. (2005). Patterns in stream longitudinal profiles and implications for hyporheic exchange flow at the H.J. Andrews Experimental Forest, Oregon, USA. *Hydrological Processes*.  
<https://doi.org/10.1002/hyp.5791>
- Bethune, J., Randell, J., Runkel, R. L., & Singha, K. (2015). Non-invasive flow path characterization in a mining-impacted wetland. *Journal of Contaminant Hydrology*.  
<https://doi.org/10.1016/j.jconhyd.2015.10.002>
- Binley, A., & Kemna, A. (2005). DC resistivity and induced polarization methods BT - Hydrogeophysics. In *Hydrogeophysics*.
- Boulton, A. J., Datry, T., Kasahara, T., Mutz, M., & Stanford, J. A. (2010). Ecology and management of the hyporheic zone: stream-groundwater interactions of running waters and their floodplains. *Journal of the North American Benthological Society*.  
<https://doi.org/10.1899/08-017.1>
- Buffington, J. M., Lisle, T. E., Woodsmith, R. D., & Hilton, S. (2002). Controls on the size and occurrence of pools in coarse-grained forest rivers. *River Research and Applications*.  
<https://doi.org/10.1002/rra.693>
- Buffington, J. M., & Tonina, D. (2009). Hyporheic exchange in mountain rivers II: Effects of channel morphology on mechanics, scales, and rates of exchange. *Geography Compass*.  
<https://doi.org/10.1111/j.1749-8198.2009.00225.x>
- Campbell, I. C., & Doeg, T. J. (1989). Impact of timber harvesting and production on streams: A review. *Marine and Freshwater Research*. <https://doi.org/10.1071/MF9890519>
- Cardenas, M. B., & Markowski, M. S. (2011). Geoelectrical imaging of hyporheic exchange and mixing of river water and groundwater in a large regulated river. *Environmental Science and Technology*. <https://doi.org/10.1021/es103438a>
- Cardenas, M. B., Wilson, J. L., & Zlotnik, V. A. (2004). Impact of heterogeneity, bed forms, and stream curvature on subchannel hyporheic exchange. *Water Resources Research*.  
<https://doi.org/10.1029/2004WR003008>
- Coscia, I., Greenhalgh, S. A., Linde, N., Doetsch, J., Marescot, L., Gu, T., ... Green, A. G. (2011). 3D crosshole ERT for aquifer characterization and monitoring of infiltrating river water. *Geophysics*. <https://doi.org/10.1190/1.3553003>
- Curran, J. H., & Wohl, E. E. (2003). Large woody debris and flow resistance in step-pool channels, Cascade Range, Washington. *Geomorphology*. [https://doi.org/10.1016/S0169-555X\(02\)00333-1](https://doi.org/10.1016/S0169-555X(02)00333-1)
- Downing, J. A., Cole, J. J., Duarte, C. M., Middelburg, J. J., Melack, J. M., Prairie, Y. T., ... Tranvik, L. J. (2012). Global abundance and size distribution of streams and rivers. *Inland*

Waters. <https://doi.org/10.5268/IW-2.4.502>

- Drummond, J. D., Covino, T. P., Aubeneau, A. F., Leong, D., Patil, S., Schumer, R., & Packman, A. I. (2012). Effects of solute breakthrough curve tail truncation on residence time estimates: A synthesis of solute tracer injection studies. *Journal of Geophysical Research: Biogeosciences*. <https://doi.org/10.1029/2012JG002019>
- Fanelli, R. M., & Lautz, L. K. (2008). Patterns of water, heat, and solute flux through streambeds around small dams. *Ground Water*. <https://doi.org/10.1111/j.1745-6584.2008.00461.x>
- Fischer, H., Kloep, F., Wilzcek, S., & Pusch, M. T. (2005). A river's liver - Microbial processes within the hyporheic zone of a large lowland river. *Biogeochemistry*. <https://doi.org/10.1007/s10533-005-6896-y>
- Gooseff, M. N., Anderson, J. K., Wondzell, S. M., LaNier, J., & Haggerty, R. (2006). A modelling study of hyporheic exchange pattern and the sequence, size, and spacing of stream bedforms in mountain stream networks, Oregon, USA. *Hydrological Processes*. <https://doi.org/10.1002/hyp.6349>
- Gupta, A., & Cvetkovic, V. (2000). Temporal moment analysis of tracer discharge in streams: Combined effect of physicochemical mass transfer and morphology. *Water Resources Research*. <https://doi.org/10.1029/2000WR900190>
- Hancock, P. J. (2002). Human impacts on the stream-groundwater exchange zone. *Environmental Management*. <https://doi.org/10.1007/s00267-001-0064-5>
- Harbaugh, Arlen, W. (2005). MODFLOW-2005 , The U . S . Geological Survey Modular Ground-Water Model — the Ground-Water Flow Process. *U.S. Geological Survey Techniques and Methods*. <https://doi.org/10.1007/s00267-001-0064-5>
- Harvey, C. F., & Gorelick, S. M. (1995). Temporal Moment-Generating Equations: Modeling Transport and Mass Transfer in Heterogeneous Aquifers. *Water Resources Research*. <https://doi.org/10.1029/95WR01231>
- Harvey, J. W., & Bencala, K. E. (1993). The Effect of streambed topography on surface-subsurface water exchange in mountain catchments. *Water Resources Research*. <https://doi.org/10.1029/92WR01960>
- Hester, E. T., & Doyle, M. W. (2008). In-stream geomorphic structures as drivers of hyporheic exchange. *Water Resources Research*. <https://doi.org/10.1029/2006WR005810>
- Jarrett, R. D. (1990). Paleohydrologic techniques used to define the spatial occurrence of floods. *Geomorphology*. [https://doi.org/10.1016/0169-555X\(90\)90044-Q](https://doi.org/10.1016/0169-555X(90)90044-Q)
- Kail, J., Hering, D., Muhar, S., Gerhard, M., & Preis, S. (2007). The use of large wood in stream restoration: Experiences from 50 projects in Germany and Austria. *Journal of Applied Ecology*. <https://doi.org/10.1111/j.1365-2664.2007.01401.x>
- Keller, G. V., & Frischknecht, F. C. (1966). *Electrical Methods in Geophysical Prospecting*. Pergamon Press, Oxford.

- LaBrecque, D. J., & Yang, X. (2009). Difference Inversion of ERT Data: a Fast Inversion Method for 3-D In Situ Monitoring. *Journal of Environmental and Engineering Geophysics*. <https://doi.org/10.4133/jeeeg6.2.83>
- Lautz, L. K., Siegel, D. I., & Bauer, R. L. (2006). Impact of debris dams on hyporheic interaction along a semi-arid stream. *Hydrological Processes*. <https://doi.org/10.1002/hyp.5910>
- Livers, B., & Wohl, E. (2016). Sources and interpretation of channel complexity in forested subalpine streams of the Southern Rocky Mountains. *Water Resources Research*. <https://doi.org/10.1002/2015WR018306>
- Loheide, S. P., & Lundquist, J. D. (2009). Snowmelt-induced diel fluxes through the hyporheic zone. *Water Resources Research*. <https://doi.org/10.1029/2008WR007329>
- Manners, R. B., Doyle, M. W., & Small, M. J. (2007). Structure and hydraulics of natural woody debris jams. *Water Resources Research*. <https://doi.org/10.1029/2006WR004910>
- Marion, A., Packman, A. I., Zaramella, M., & Bottacin-Busolin, A. (2008). Hyporheic flows in stratified beds. *Water Resources Research*. <https://doi.org/10.1029/2007WR006079>
- Marzadri, A., Tonina, D., Bellin, A., Vignoli, G., & Tubino, M. (2010). Semianalytical analysis of hyporheic flow induced by alternate bars. *Water Resources Research*. <https://doi.org/10.1029/2009WR008285>
- Millington, C. E., & Sear, D. A. (2007). Impacts of river restoration on small-wood dynamics in a low-gradient headwater stream. *Earth Surface Processes and Landforms*. <https://doi.org/10.1002/esp.1552>
- Palmer, M. A., Menninger, H. L., & Bernhardt, E. (2010). River restoration, habitat heterogeneity and biodiversity: A failure of theory or practice? *Freshwater Biology*. <https://doi.org/10.1111/j.1365-2427.2009.02372.x>
- Poff, N. L., Olden, J. D., Merritt, D. M., & Pepin, D. M. (2007). Homogenization of regional river dynamics by dams and global biodiversity implications. *Proceedings of the National Academy of Sciences*. <https://doi.org/10.1073/pnas.0609812104>
- Salehin, M., Packman, A. I., & Paradis, M. (2004). Hyporheic exchange with heterogeneous streambeds: Laboratory experiments and modeling. *Water Resources Research*. <https://doi.org/10.1029/2003WR002567>
- Sawyer, A. H., Bayani Cardenas, M., & Buttle, J. (2011). Hyporheic exchange due to channel-spanning logs. *Water Resources Research*. <https://doi.org/10.1029/2011WR010484>
- Sawyer, A. H., & Cardenas, M. B. (2012). Effect of experimental wood addition on hyporheic exchange and thermal dynamics in a losing meadow stream. *Water Resources Research*. <https://doi.org/10.1029/2011WR011776>
- Sear, D. A., Millington, C. E., Kitts, D. R., & Jeffries, R. (2010). Logjam controls on channel:floodplain interactions in wooded catchments and their role in the formation of multi-channel patterns. *Geomorphology*. <https://doi.org/10.1016/j.geomorph.2009.11.022>
- Sedell, J. R., Leone, F. N., & Duval, W. S. (1991). Water transportation and storage of logs.

- Singha, K., & Gorelick, S. M. (2005). Saline tracer visualized with three-dimensional electrical resistivity tomography: Field-scale spatial moment analysis. *Water Resources Research*. <https://doi.org/10.1029/2004WR003460>
- Singha, K., Pidlisecky, A., Day-Lewis, F. D., & Gooseff, M. N. (2010). Electrical characterization of non-Fickian transport in groundwater and hyporheic systems. *Water Resources Research*. <https://doi.org/10.1029/2008WR007048>
- Slater, L. D., Ntarlagiannis, D., Day-Lewis, F. D., Mwakanyamale, K., Versteeg, R. J., Ward, A., ... Lane, J. W. (2010). Use of electrical imaging and distributed temperature sensing methods to characterize surface water-groundwater exchange regulating uranium transport at the Hanford 300 Area, Washington. *Water Resources Research*. <https://doi.org/10.1029/2010WR009110>
- Sweeney, B. W., & Newbold, J. D. (2014). Streamside forest buffer width needed to protect stream water quality, habitat, and organisms: A literature review. *Journal of the American Water Resources Association*. <https://doi.org/10.1111/jawr.12203>
- Tonina, D., & Buffington, J. M. (2007). Hyporheic exchange in gravel bed rivers with pool-riffle morphology: Laboratory experiments and three-dimensional modeling. *Water Resources Research*. <https://doi.org/10.1029/2005WR004328>
- Tonina, D., & Buffington, J. M. (2009). Hyporheic exchange in mountain rivers I: Mechanics and environmental effects. *Geography Compass*. <https://doi.org/10.1111/j.1749-8198.2009.00226.x>
- Tonina, D., & Buffington, J. M. (2011). Effects of stream discharge, alluvial depth and bar amplitude on hyporheic flow in pool-riffle channels. *Water Resources Research*. <https://doi.org/10.1029/2010WR009140>
- Toran, L., Hughes, B., Nyquist, J., & Ryan, R. (2012). Using hydrogeophysics to monitor change in hyporheic flow around stream restoration structures. *Environmental and Engineering Geoscience*. <https://doi.org/10.2113/gsegeosci.18.1.83>
- Toran, L., Nyquist, J. E., Fang, A. C., Ryan, R. J., & Rosenberry, D. O. (2013). Observing lingering hyporheic storage using electrical resistivity: Variations around stream restoration structures, Crabby Creek, PA. *Hydrological Processes*. <https://doi.org/10.1002/hyp.9269>
- Ward, A. S., Gooseff, M. N., Fitzgerald, M., Voltz, T. J., & Singha, K. (2014). Spatially distributed characterization of hyporheic solute transport during baseflow recession in a headwater mountain stream using electrical geophysical imaging. *Journal of Hydrology*. <https://doi.org/10.1016/j.jhydrol.2014.05.036>
- Ward, A. S., Gooseff, M. N., & Singha, K. (2010a). Characterizing hyporheic transport processes - Interpretation of electrical geophysical data in coupled stream-hyporheic zone systems during solute tracer studies. *Advances in Water Resources*. <https://doi.org/10.1016/j.advwatres.2010.05.008>
- Ward, A. S., Gooseff, M. N., & Singha, K. (2010b). Imaging hyporheic zone solute transport using electrical resistivity. *Hydrological Processes*. <https://doi.org/10.1002/hyp.7672>

- Wohl, E. (2005). Compromised rivers: Understanding historical human impacts on rivers in the context of restoration. *Ecology and Society*. <https://doi.org/10.5751/ES-01339-100202>
- Wohl, E. (2017). The significance of small streams. *Frontiers of Earth Science*. <https://doi.org/10.1007/s11707-017-0647-y>
- Wohl, E., & Beckman, N. (2014). Controls on the longitudinal distribution of channel-spanning logjams in the Colorado front range, USA. *River Research and Applications*. <https://doi.org/10.1002/rra.2624>
- Wohl, E., & Goode, J. R. (2008). Wood dynamics in headwater streams of the Colorado Rocky Mountains. *Water Resources Research*. <https://doi.org/10.1029/2007WR006522>
- Wohl, E., & Scott, D. N. (2017). Wood and sediment storage and dynamics in river corridors. *Earth Surface Processes and Landforms*. <https://doi.org/10.1002/esp.3909>
- Wondzell, S. M. (2006). Effect of morphology and discharge on hyporheic exchange flows in two small streams in the Cascade Mountains of Oregon, USA. *Hydrological Processes*. <https://doi.org/10.1002/hyp.5902>
- Wörman, A., Packman, A. I., Johansson, H., & Jonsson, K. (2002). Effect of flow-induced exchange in hyporheic zones on longitudinal transport of solutes in streams and rivers. *Water Resources Research*. <https://doi.org/10.1029/2001WR000769>
- Wroblicky, G. J., Campana, M. E., Valett, H. M., & Dahm, C. N. (1998). Seasonal variation in surface-subsurface water exchange and lateral hyporheic area of two stream-aquifer systems. *Water Resources Research*. <https://doi.org/10.1029/97WR03285>

APPENDIX A

SUPPORTING FIGURES

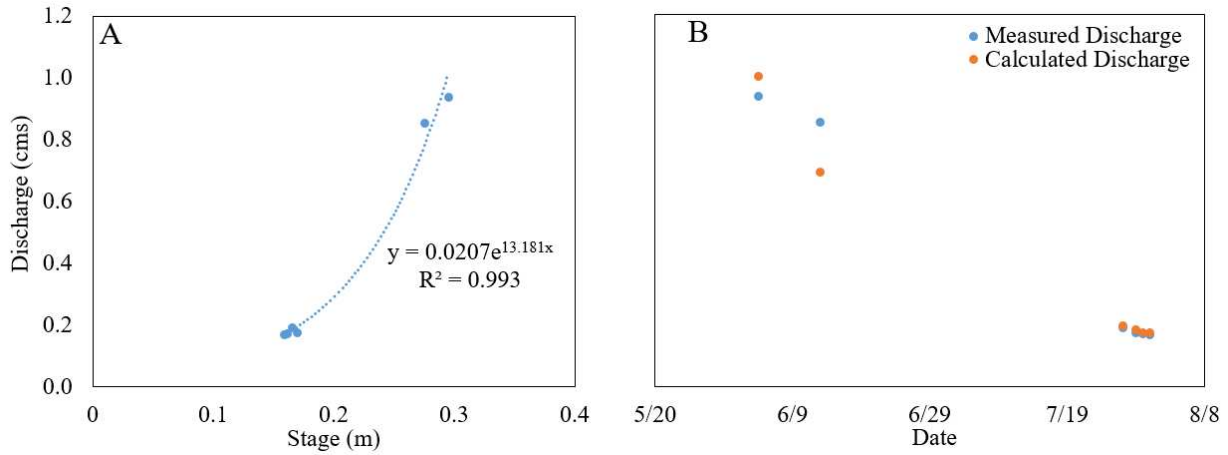


Figure A.1 (A) Developed rating curve from stream gauging and stage measurements at the stilling well. (B) A comparison of the measured and calculated discharge.

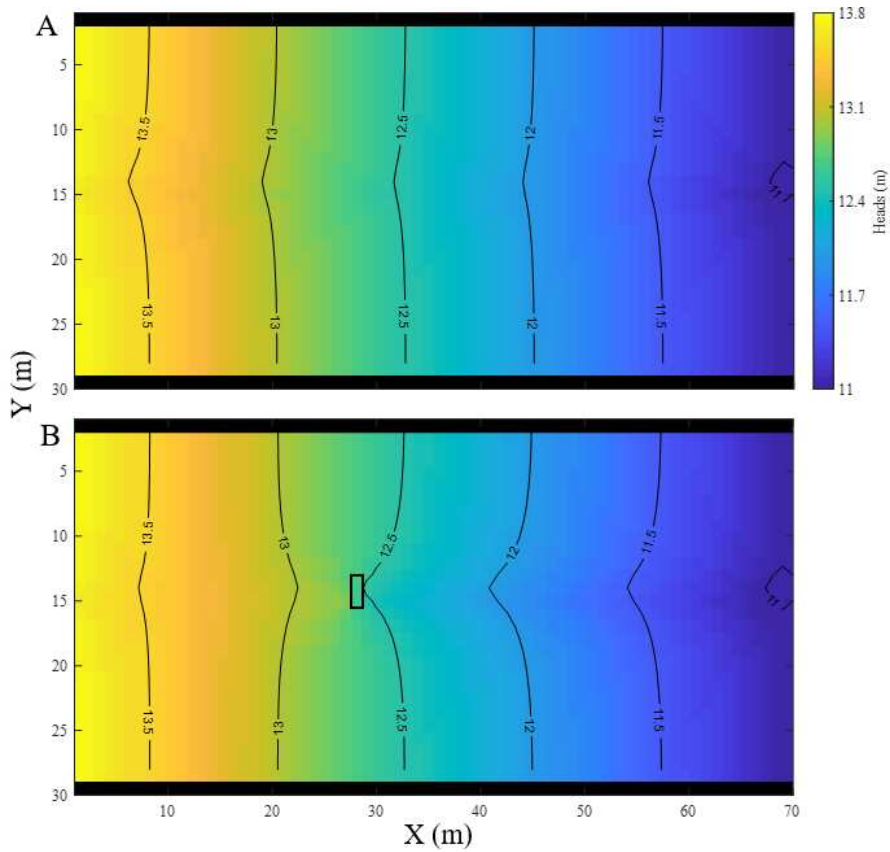


Figure A.2 Head distribution maps of (A) no-logjam, high-flow model and (B) logjam, high-flow model at Z = 0 m. The black outlined boxed represents the location of the logjam.

Table A.1 Temporal Moment Calculations for Fluid Conductivity

	June 13-14			July 10-11			July 28-29		
	Control	Above Jam	Below Jam	Control	Above Jam	Below Jam	Control	Above Jam	Below Jam
Mass (kg)	328	204	356	66	--	65	92	99	96
Mean Arrival Time (hr)	2	2	2	2	--	2	3	2	2
Variance (hr <sup>2</sup> )	4	5	7	2	--	3	4	3	3
Skewness	39	53	87	18	--	36	38	13	13

Table A.2 Temporal Moment Calculations for Bulk Conductivity

	June 13-14			July 10-11			July 28-29		
	Control	Above Jam	Below Jam	Control	Above Jam	Below Jam	Control	Above Jam	Below Jam
Mass (kg)	225	89	91	42	12	17	52	12	17
Mean Arrival Time (hr)	7	6	5	9	8	8	11	10	9
Variance (hr <sup>2</sup> )	36	32	29	42	40	42	50	58	63
Skewness	204	225	225	120	185	181	209	367	535

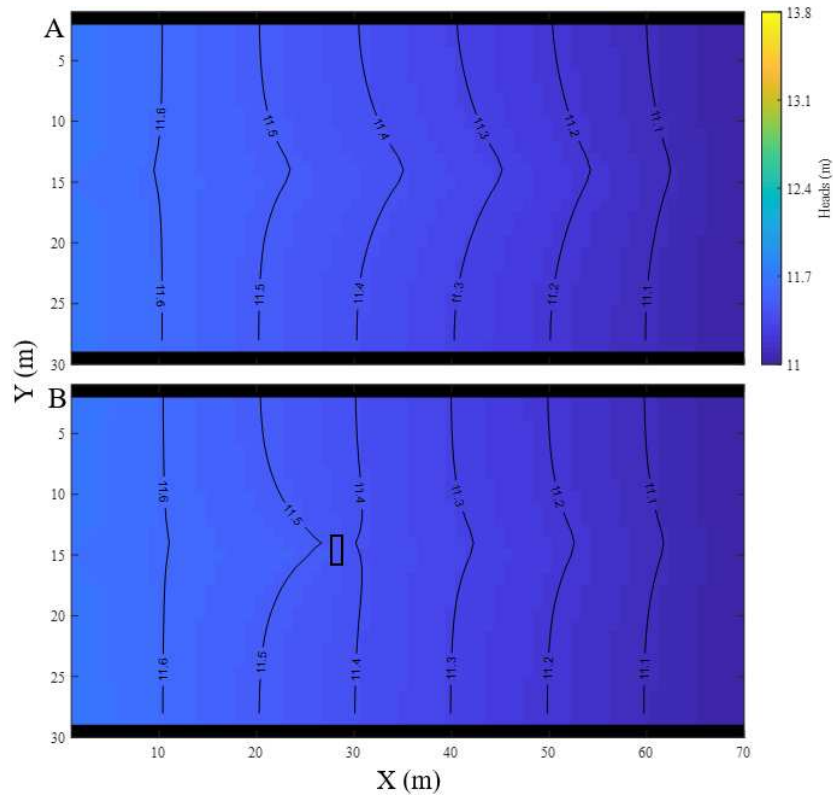


Figure A.3 Head distribution maps of (A) no-logjam, low-flow model and (B) logjam, low-flow model at  $Z = 0$  m. The black outlined boxed represents the location of the logjam.

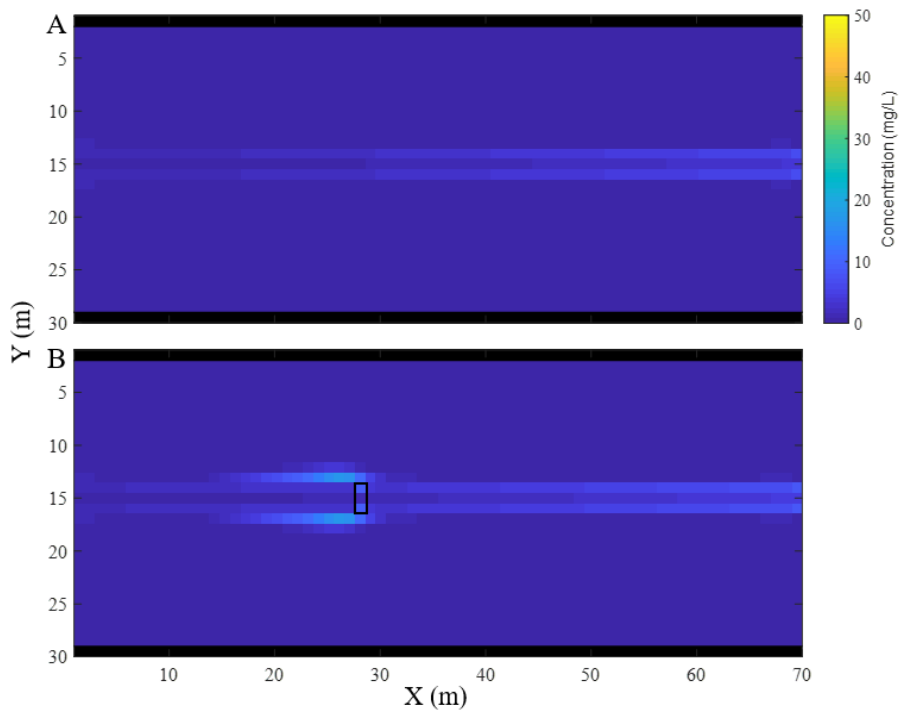


Figure A.4 Map view of the concentration plot for (A) no-logjam, high-flow model and (B) logjam, high-flow model at  $Z = 0$  m. This is 4 hours after the tracer ended.

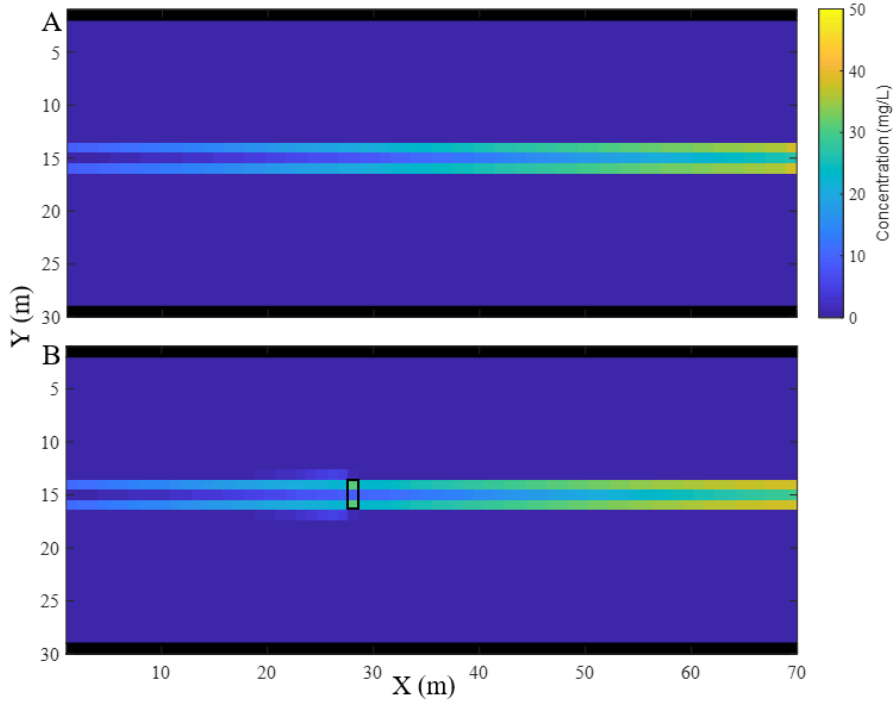


Figure A.5 Map view of the concentration plot for (A) no-logjam, low-flow model and (B) logjam, low-flow model at  $Z = 0$  m. This is 4 hours after the tracer ended.

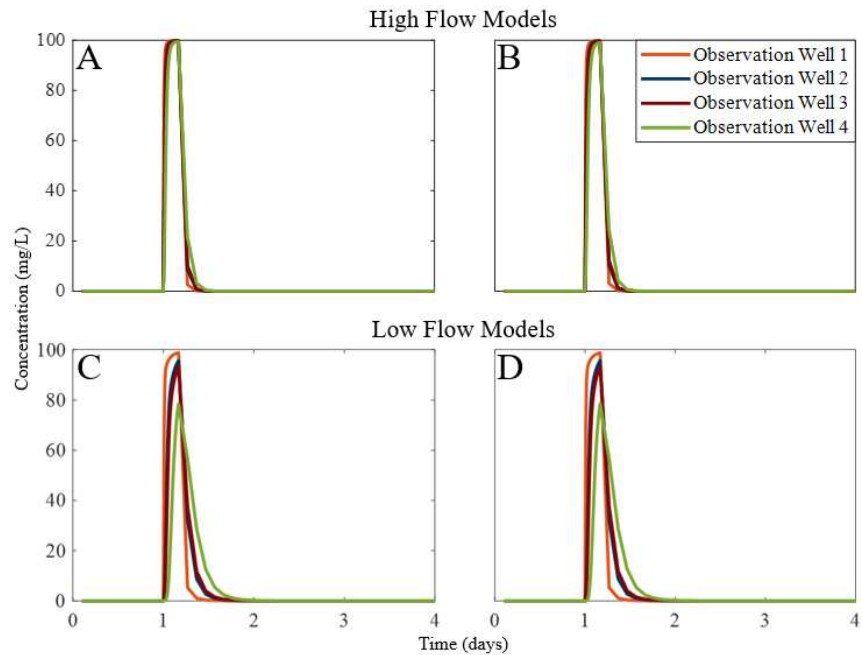


Figure A.6 Concentration (mg/L) in stream from the four models at the four observation wells: (A) No-logjam, high-flow, (B) Logjam, high-flow, (C) No-logjam, low-flow, (D) Logjam, low-flow. The location of the observation wells is shown in the model configuration. Observation well 1 is at the beginning of the model, well 2 is right before Site A, well 3 is right after Site B, and well 4 is at the end of the mode.

Table A.3 Site A, Site B, and Site C Temporal Moments for the four model configurations. For any cell that never reached a concentration over 0.005 mg/L, the temporal moments were not calculated.

Site A												
	No Logjam, High Flow			Logjam, High Flow			No Logjam, Low Flow			Logjam, Low Flow		
Cell	1	2	3	1	2	3	1	2	3	1	2	3
Mass (kg)	1469	31	153	1246	1304	1266	308	5	27	280	295	290
Mean Arrival Time (hr)	3	--	111	3	62	28	8	--	360	8	232	95
Variance (hr <sup>2</sup> )	5	--	7.13*10 <sup>3</sup>	8	4.81*10 <sup>3</sup>	916	27	--	7.30*10 <sup>4</sup>	32	6.17*10 <sup>4</sup>	1.08*10 <sup>4</sup>
Skewness	20	--	5.60*10 <sup>5</sup>	123	8.68*10 <sup>5</sup>	7.97*10 <sup>4</sup>	178	--	1.49*10 <sup>7</sup>	252	3.19*10 <sup>7</sup>	2.7610 <sup>6</sup>
Site B												
Mass (kg)	1467	34	179	1260	1339	1331	308	0	32	280	292	294
Mean Arrival Time (hr)	3	--	128	6	106	43	8	--	428	25	426	164
Variance (hr <sup>2</sup> )	5	--	9.33*10 <sup>3</sup>	405	8.34*10 <sup>3</sup>	1.42*10 <sup>3</sup>	28	--	1.02*10 <sup>5</sup>	6.74*10 <sup>3</sup>	1.21*10 <sup>5</sup>	2.08*10 <sup>4</sup>
Skewness	20	--	8.29*10 <sup>5</sup>	6.46*10 <sup>4</sup>	1.68*10 <sup>6</sup>	1.42*10 <sup>5</sup>	181	--	2.42*10 <sup>7</sup>	3.43*10 <sup>6</sup>	7.29*10 <sup>7</sup>	6.74*10 <sup>6</sup>
Site C												
Mass (kg)	1439	29	222	1231	423	404	309	0	72	280	0	63
Mean Arrival Time (hr)	4	--	226	4	1.01*10 <sup>3</sup>	391	9	--	854	10	--	1.17*10 <sup>3</sup>
Variance (hr <sup>2</sup> )	6	--	4.03*10 <sup>4</sup>	7	1.15*10 <sup>5</sup>	6.51*10 <sup>4</sup>	28	--	3.60*10 <sup>5</sup>	33	--	4.51*10 <sup>5</sup>
Skewness	23	--	7.93*10 <sup>6</sup>	33	-2.05*10 <sup>7</sup>	1.65*10 <sup>7</sup>	176	--	1.28*10 <sup>8</sup>	247	--	-6.71*10 <sup>7</sup>

## APPENDIX B

### TEMPORAL MOMENT CALCULTIONS: MATLAB FUNCTION

```
function [M0, mat, var, skew]= tempMO(conc, time)
%input arguments are concentration or EC data and corresponding times

%removing numbers that start before the injection
after_inj=find(time>1);
time_inj=time(after_inj);
conc_inj=conc(after_inj);

%find time elapsed
elaps_time=(time_inj-time_inj(1))*24; %time in hours

dt(1)=elaps_time(1);
for i=2:length(elaps_time)-1
    dt(i)= elaps_time(i)-elaps_time(i-1);
end

%Calculate the zeroth moment for each time measurement
for i=1:length(elaps_time)
    it_0(i)=(elaps_time(i)^0)*conc_inj(i);
end

%Using trapezoidal integration for the zeroth moments
M0=0;
for i=1:length(elaps_time)-1
    M0=M0 + ((it_0(i)+it_0(i+1))*0.5*dt(i));
end

%Calculate the first moment for each time measurement
for i=1:length(elaps_time)
    it_1(i)=(elaps_time(i)^1)*conc_inj(i);
end

%Using trapezoidal integration for the first moments
M1=0;
for i=1:length(elaps_time)-1
    M1=M1+ ((it_1(i)+it_1(i+1))*0.5*dt(i));
end

%Calculate the second moment for each time measurement
for i=1:length(elaps_time)
    it_2(i)=(elaps_time(i)^2)*conc_inj(i);
```

```

end

%Using trapezoidal integration for the second moments
M2=0;
for i=1:length(elaps_time)-1
    M2=M2+ ((it_2(i)+it_2(i+1))*0.5*dt(i));
end

%Calculate the third moment for each time measurement
for i=1:length(elaps_time)
    it_3(i)=(elaps_time(i)^3)*conc_inj(i);
end

%Using trapezoidal integration for the second moments
M3=0;
for i=1:length(elaps_time)-1
    M3=M3+ ((it_3(i)+it_3(i+1))*0.5*dt(i));
end

mat=M1/M0; %calculation of the mean arrival time
var=(M2/M0)-(mat^2); %calculations of the variance
skew=(M3/M0)-(3*var*mat)-(mat^3); %calculation of the skew

end

```